1 **Revision 2 of**
2 **Pyrite trace element and sulphur isotope geochemistry of Paleo-Mesoproterozoic**
3 **McArthur Basin: Proxy for Oxidative weathering**
4

5 Indrani Mukherjee[1*], Ross R Large[1], Stuart Bull[1], Daniel G Gregory[2], Aleksandr S.
6 Stepanov[1], Janaína Ávila[3], Trevor. R. Ireland[3] and Ross Corkrey[4]
7

8 *1. Centre for Ore Deposit and Earth Sciences (CODES), University of Tasmania, Private*
9 *Bag 126, Hobart, Tasmania 7001, Australia*
10

11 *2. Department of Earth Sciences, University of California, Riverside, CA 92521, USA*
12

13 *3. Research School of Earth Sciences, The Australian National University, Canberra, ACT*
14 *2601, Australia*
15

16 *4. Tasmanian Institute of Agricultural Research (TIAR), University of Tasmania, Hobart,*
17 *Tasmania 7001, Australia*
18

19 **Corresponding author: Indrani Mukherjee, email: Indrani.Mukherjee@utas.edu.au*
20
21
22

23 **Abstract:** Redox sensitive trace elements and sulphur isotope compositions obtained via in-

24 situ analyses of sedimentary pyrites from marine black shales, are used to track atmosphere-

25 ocean redox conditions between ~1730 and ~1360 Ma in the McArthur Basin, northern

26 Australia. Three black shale formations within the basin, (Wollogorang Formation 1730 $\pm$ 3

27 Ma, Barney Creek Formation 1640 $\pm$ 3 Ma and Upper Velkerri Formation 1361 $\pm$ 21 Ma)

28 display systematic stratigraphic variations in pyrite trace element compositions obtained

29 using LA-ICP-MS. The concentrations of several trace elements and their ratios, such as Se,

30 Zn, Se/Co, Ni/Co, Zn/Co, Mo/Co, Se/Bi, Zn/Bi, Ni/Bi, increase from the stratigraphically

31 lower Wollogorang Formation to the Upper Velkerri Formation. Cobalt, Bi, Mo, Cu and Tl,

32 show a consistent decrease in abundance while Ni, As and Pb show no obvious trends.

33

34 We interpret these trace element trends as a response to the gradual increase of oxygen in the

35 atmosphere-ocean system from ~1730 to 1360 Ma. Elements more mobile during erosion

36 under rising atmospheric oxygen show an increase up stratigraphy (e.g. Zn, Se) whereas

37 elements that are less mobile show a decrease (e.g. Co, Bi). We also propose the increase of

38 elemental ratios (Se/Co, Ni/Co, Zn/Co, Mo/Co, Ni/Bi and Zn/Bi) up stratigraphy are strong

39 indicators of atmospheric oxygenation.

40

41 Sulphur isotopic compositions of marine pyrite ($\delta^{34}S_{pyrite}$) from these formations, obtained

42 using SHRIMP-SI, are highly variable, with the Wollogorang Formation exhibiting less

43 variation ($\delta^{34}S$ = –29.4 to +9.5‰; mean: –5.03‰) in comparison to the Barney Creek ($\delta^{34}S$ =

44 –13.8 to +41.8‰; mean: +19.88‰) and Velkerri Formations ($\delta^{34}S$ = –14.2 to +52.8‰; mean:

45 +26.9‰). We propose that the shift in mean $\delta^{34}S$ to heavier values upsection corresponds to

46 increasing deep water oxygenation from ~1730 to 1360 Ma. Incursion of oxygenated waters

47 possibly caused a decrease in the areal extent of anoxic areas, at the same time, creating a

48 possibly efficient reducing system. A stronger reducing system caused the $\delta^{34}S$ of the

49 sedimentary pyrites to become progressively heavier. Interestingly, heavy $\delta^{34}S$ in pyrites

50 overlaps with the increase in the concentration of certain trace elements (and their ratios) in

51 sedimentary pyrites (Se, Zn, Se/Co, Ni/Co, Zn/Co, Mo/Co, Ni/Bi and Zn/Bi). This study

52 concludes that there was a gradual increase of atmospheric oxygen accompanied by ocean

53 oxygenation through the first ~400 million years of the Boring Billion (1800-1400 Ma) in the

54 McArthur Basin.

55

56 **INTRODUCTION**

57

58 Sedimentary rocks of the McArthur Basin in northern Australia have been the focus of

59 various studies on the application of bio-geochemical techniques to understand ocean and

60 atmospheric redox conditions during the Paleo-Mesoproterozoic. These sedimentary

61 packages are unmetamorphosed, relatively undeformed and believed to preserve imprints of

62   the biological and geochemical processes operative during their deposition (Brasier et al.,

63   1998; Anbar and Knoll, 2002; Shen et al., 2002; Arnold et al., 2004; Brocks et al., 2005;

64   Javaux et al., 2001, 2004; Scott et al., 2008; Johnston et al., 2008; Kendall et al., 2009;

65   Planavsky et al., 2011; Planavsky et al.., 2014; Lyons et al., 2014; Large et al., 2014).

66   Particular interest in the McArthur Basin arises because it provides an insight into the

67   "Boring Billion" period (1800-800 Ma), which has been of great interest since being referred

68   to as "one of the dullest period in Earth's history" (Buick, 1995) and as "a billion year of

69   environmental stasis" (Brasier and Lindsay, 1998). Several techniques have been used to

70   decipher the depositional conditions in order to interpret basin redox structure and its impact

71   on biological processes. Isotopic (C, Sr, S, Mo, Cr) and biomarker studies have been

72   undertaken to provide an overall perspective on the McArthur Basin redox conditions

73   (Brasier and Lindsay; 1998; Lindsay and Brasier, 2000; Shen et al., 2002; Chen et al., 2003;

74   Kah et al., 2004; Brocks et al., 2005; Johnston et al., 2008; Scott et al., 2008; Planavsky et al.,

75   2014; Luo et al., 2015). Bulk rock trace element concentrations in sedimentary rocks,

76   particularly black shales and ironstones, have also enhanced our understanding of Proterozoic

77   ocean biogeochemistry (Lyons et al., 2003; Tribovillard et al., 2006; Konhauser et al., 2009;

78   Sahoo et al., 2012; Reinhard et al., 2013; Partin et al., 2013; Planavsky et al., 2014).

79   Recently, studies by Large et al. (2014), Large et al. (2015 a, b), Gregory et al. (2014, 2015a,

80   2017), and Mukherjee and Large (2016, 2017) have shown that trace element concentrations

81   in marine sedimentary pyrite from black shales can also be used to infer ocean-atmosphere

82   redox relationships. Using the technique introduced by Large et al., (2014), potential

83   oxygenation during the Velkerri Formation depositional period (~1360 Ma) has been

84   proposed (Mukherjee and Large, 2016) on the basis of enrichment of certain redox sensitive

85   trace elements (Se, Mo, Ni, Zn) in pyrite in the black shales.

86

87　　The aim of the present contribution is to further our understanding of marine conditions

88　　(redox state of the atmosphere and ocean, nutrient trace element availability) in the McArthur

89　　Basin by measuring trace element concentrations and S isotopic compositions of marine

90　　pyrite in three black shale formations from the McArthur basin stratigraphy. These are the

91　　Velkerri Formation (~1400 Ma), Barney Creek Formation (~1650 Ma) and Wollogorang

92　　Formation (~1730 Ma) located in in the Roper, McArthur and Tawallah Groups respectively.

93

94　　The McArthur Basin was chosen for this study for several reasons. First, the basin is a

95　　multiphase tectonic system with five coherent packages (Wilton, Favenc, Glyde, Goyder and

96　　Redbank), each with a characteristic age, lithostratigraphy, volcanism (style and

97　　composition), basin architecture and micropaleontology (Rawlings, 1999). Of the five

98　　packages, three comprise marine black shale formations, which makes the McArthur Basin

99　　an ideal location to apply the technique introduced by Large et al. (2014; 2017), of using

100　　trace element concentrations of sedimentary pyrite in marine black shales to infer redox

101　　conditions of the ocean and atmosphere. The McArthur also provides an opportunity to

102　　investigate possible factors such as atmosphere-ocean redox and basin tectonics that

103　　controlled the pyrite trace element concentrations. Second, previous studies (Bull, 1998;

104　　Jackson et al., 2000; Shen et al., 2002; Brocks et al., 2008; Johnston et al., 2008; Kendall et

105　　al., 2009) have shown that the intracratonic McArthur Basin was connected to the global

106　　ocean, possibly allowing us to infer global redox conditions between 1730 Ma and 1360 Ma.

107

108　　**Importance of combining sedimentary pyrite trace element and sulphur isotope**

109　　**compositions**

110

111   Certain redox-sensitive trace elements (Mo, U, Cr, V, Zn) in black shales have been used

112   previously as paleoredox indicators of the water column (Algeo et al., 2006; Tribovillard et

113   al., 2006; Algeo et al., 2009; Algeo et al., 2012; Meyer et al., 2008; Gordon et al., 2009;

114   Sahoo et al., 2012; Sahoo et al., 2016). Also, they have been used to track atmospheric

115   oxygenation through time (Scott et al., 2008; Partin et al., 2013; Lyons et al., 2014).

116   Recently, Large et al. (2014) proposed that trace element concentrations in sedimentary

117   pyrite formed in marine black shales could also be used as proxies for ocean trace element

118   chemistry and atmospheric oxygenation. The pyrite technique relies on the fact that most

119   redox-sensitive trace elements, in bottom waters and pore waters, are readily and efficiently

120   incorporated into sedimentary pyrites (Huerta-Diaz and Morse, 1992; Morse and Arakaki,

121   1993, Rickard et al., 2012; Gregory et al., 2014; Large et al., 2014; Gregory et al., 2015a;

122   Mukherjee and Large, 2016, 2017). The premise on which the technique is based is that

123   enhanced oxidative weathering on land causes an increase in the supply of redox-sensitive

124   trace elements in the riverine flux (dominant source) in the ocean (Bertine and Turekian,

125   1973; Taylor and McLennan, 1995; Scott et al., 2008; Sahoo et al., 2012; Crowe et al., 2013).

126   This is coupled with a decrease in areal extent of sulfidic bottom waters, a main sink for

127   several trace elements (Sahoo et al., 2016). On encountering a redox-boundary, these trace

128   elements become readily adsorbed by sedimentary pyrites forming in anoxic black shales,

129   either in the water column or in the upper most part of the sediments. Hence, an increase in

130   concentrations of redox sensitive trace elements in sedimentary pyrites can act as an indirect

131   proxy for an increase in atmospheric oxygenation (Gregory et al., 2014; Large et al., 2014;

132   Gregory et al., 2015a; Mukherjee and Large, 2016; 2017).

133

134   Bulk-rock sulphur isotope compositions of the McArthur Basin sediments have been studied

135   previously (Donnelly and Crick, 1988; Canfield, 1998; Shen et al., 2002; Shen et al., 2003;

136   Kah et al., 2004; Lyons et al., 2006; Johnston et al., 2008). Those studies produced $^{34}S/^{32}S$

137   compositions but additional information on depositional environment, microbial activity and

138   connectivity to the global ocean can be obtained using isotopes such as ^{33}S and ^{36}S

139   abundances (Johnston et al., 2008). Sulphur isotopic compositions of the McArthur Basin

140   sediments have also been reported previously to understand changes in sea water sulphate

141   concentration and the sulphate reservoir, biogeochemical sulphur isotope fractionation

142   patterns, global oxidative sulphur cycling and redox stratification of the Proterozoic oceans

143   (Shen et al., 2002; Kah et al., 2004; Johnston et al., 2008; Luo et al., 2015). In this study, we

144   carried out sulphur isotope analyses of sedimentary pyrites with SHRIMP-SI (Ireland, 2008)

145   and combined them with trace element concentrations to provide additional insight into

146   changes in putative biogeochemical processes operative during the deposition of the three

147   black shales formations.

148

149   There are several advantages of using a combined marine pyrite trace element (TE) and S-

150   isotope approach for understanding ocean chemistry. First, both techniques offer high spatial

151   resolution, so measurements can be performed within a single grain domain, avoiding the

152   problem of differing amounts of the detrital component that may adversely affect whole rock

153   analyses. Many TE, such as Mo, are partitioned between minerals in the shale (Tribovillard et

154   al., 2006), and thus variations in mineral composition can affect the bulk rock analyses

155   (Chappaz et al., 2014). Second, the effects of diagenesis, metamorphism and hydrothermal

156   activity, all of which affect trace element concentrations and sulphur isotopic compositions,

157   can be identified by textural studies of the pyrite (Large et al., 2014). For example, Large et

158   al. (2007; 2009) demonstrated that recrystallization of pyrite during metamorphism releases

159   most trace elements and results in subhedral to euhedral forms of pyrite with low trace

160   element abundances. Hydrothermal pyrites, on the other hand, may be enriched or depleted in

161   trace elements depending on the conditions of formation (temperature, salinity, proximity to

162   vents). These hydrothermal pyrite concentrations therefore do not reflect primary trace

163   element concentrations of the sea water (Large et al., 2014; Mukherjee and Large, 2017).

164

165   **GEOLOGICAL SETTING**

166

167   The McArthur Basin, northern Australia, preserves a Paleo-Mesoproterozoic volcano-

168   sedimentary history (Plumb, 1979a, b; Rawlings et al., 1999) (Fig. 1). The basin is divided

169   into northern and southern elements by the roughly east-west trending Urapunga Fault zone.

170   Both basin elements comprise a central N-S trending element (Walker and Batten Fault Zone

171   respectively) with flanking "shelves". For this paper, we will refer to the stratigraphy of

172   southeastern part of the Batten Fault Zone, in which the basin fill is divided into four major

173   groups (Tawallah, McArthur, Nathan and Roper, Figure 1). With the exception of the Nathan

174   Group, each includes black shale formations i.e., Wollogorang Formation, Barney Creek

175   Formation, and Velkerri Formation in the Tawallah, McArthur, and Roper Groups

176   respectively (Fig. 2).

177

178   **Stratigraphy and depositional environments of the three black shale formations**

179

180   *Wollogorang Formation*

181

182   The Wollogorang Formation was deposited 1730 Ma $\pm$ 4 Ma based on U-Pb zircon ages from

183   interbedded tuffs (Page et al., 2000). It is 100-150 m thick and is divided into upper and

184   lower units on the basis of lithology. The upper Wollogorang Formation comprises mudstone

185   and dolomitic sandstone whereas the lower part of the formation consists of black shales and

186   dolomitic siltstone (Jackson et al., 1985; Donnelly and Jackson, 1988). The Wollogorang

187   Formation black shales is interpreted to be deposited in a low sulphate, marine intracratonic

188   basin with oxic surface waters and euxinic deep water conditions prevalent during deposition

189   (Jackson et al., 2000; Page et al., 2000; Southgate et al., 2000; Shen et al., 2002).

190

191   *Barney Creek Formation*

192

193   The Barney Creek Formation has a depositional age of 1640 ± 3 Ma (Page and Sweet, 1998).

194   It is divided into the Cooley Dolostone member, W-Fold Shale member and HYC Pyritic

195   Shale member (~100 m). The HYC Pyritic Shale member consists of laminated pyritic,

196   dolomitic carbonaceous siltstone/mudstone and minor tuffaceous mudstone. The black shales

197   of the Barney Creek Formation were deposited in an anoxic environment, in a subsiding

198   basin in which morphological traps were forming due to local contemporaneous vertical

199   tectonism (Bull, 1998).

200

201   *Velkerri Formation*

202

203   The Velkerri Formation is 330 m thick and is composed dominantly of black carbonaceous

204   mudstones with minor grey siltstones and very fine-grained sandstones along with minor

205   calcite nodules, pyritic stringers and glauconitic siltstones (Abbott et al., 2000). The Velkerri

206   is essentially unmetamorphosed and is relatively undeformed. The depositional age of the

207   Velkerri Formation is 1361 $\pm$ 21 Ma for the Upper Velkerri Formation and 1417 $\pm$ 29 Ma for

208   the Lower Velkerri Formation based on according to Re-Os dating (Kendall et al., 2009). The

209   Velkerri Formation black shales were deposited in a low energy offshore environment

210   (Abbott et al., 2000) as a result of hemipelagic sedimentation under anoxic conditions with

211   cyanobacterial and algal biotic communities as the source of organic matter (Crick et al.,

212   1988; Javaux et al., 2001; Gorter and Grey, 2012).

213

214   **MATERIALS AND METHOD**

215

216   **Sampling Rationale**

217

218   The black shale units of these three formations were chosen for the present study after

219   considering their similarity in lithology (organic-matter rich shales; TOC% & their

220   depositional environments) and importantly, their stratigraphic position (black shales of three

221   different ages). The varying stratigraphic positions will allow the tracking of changes in

222   ocean chemistry. (See Appendix 1 (A1.1); Table A1). Mineralogically, they are similar

223   except that both the Wollogorang and Barney Creek Formations are associated with

224   carbonates while the Velkerri Formation is not (Ahmad et al., 2013).

225

226   **Sample details**

227

228   Only drill core samples were used for the present study (Fig. 1, 3). Samples were obtained

229   from Mt Young 2, MBXDD001 and URAPUNGA-4 drill holes for Wollogorang, Barney

230   Creek and Velkerri Formations, respectively (Fig. 2). The Mount Young 2 (located in the

231   Batten fault zone) and Urapunga 4 (in the Roper Bar area – Urapanga fault zone according to

232   the map) drill cores were provided by Geoscience Australia. The MBXDD001 drill core was

233   provided by the Northern Territory Geological Survey (NTGS) drill core facility.

234   Considering that the Barney Creek Formation hosts the McArthur River SEDEX deposit, the

235   drillhole (MBXDD001) farthest away (~60 km south of the deposit) from the ore body was

236   selected in order to minimize possible effects of hydrothermal fluids (Mukherjee and Large,

237   2017). Black were selected from all three drill cores. Samples were collected every ~10 m

238   down-hole and rock chips from each interval were set in 2.5 cm diameter epoxy mounts and

239   polished with 1-micron diamond paste. Polished laser mounts were examined using reflected

240   light microscope.

241

242   **LA-ICP-MS pyrite trace element analyses**

243

244   The LA-ICP-MS analyses of trace elements in pyrite and the black shale matrix were

245   conducted at CODES, University of Tasmania. Analyses were carried out using a New Wave

246   Research UP-193ss laser microprobe coupled to an Agilent 7700s quadrupole ICP-MS for the

247   following elements and their respective isotopes, ^{13}C, ^{23}Na, ^{24}Mg, ^{27}Al, ^{29}Si, ^{34}S, ^{39}K, ^{43}Ca,

248   ^{49}Ti, ^{51}V, ^{53}Cr, ^{55}Mn, ^{57}Fe, ^{59}Co, ^{60}Ni, ^{65}Cu, ^{66}Zn, ^{75}As, ^{77}Se, ^{85}Rb, ^{88}Sr, ^{90}Zr, ^{95}Mo, ^{107}Ag,

249   ^{111}Cd, ^{118}Sn, ^{121}Sb, ^{125}Te, ^{137}Ba, ^{157}Gd, ^{178}Hf, ^{181}Ta, ^{182}W, ^{195}Pt, ^{197}Au, ^{202}Hg, ^{205}Tl, ^{206}Pb,

250   ^{207}Pb, ^{208}Pb, ^{209}Bi, ^{232}Th and ^{238}U. STGL2b2 (in-house reference material for calibration of

251   relative element sensitivities; Danyushevsky et al., 2011), GSD-1G (USGS reference glass;

252   Jochum et al., 2005) and a stoichiometric pyrite PPP-1 crystal (Gilbert et al., 2014) were the

253   three primary reference materials used to quantify the abundances of chalcophile elements,

254   lithophile elements, and sulphur abundances, respectively. All three reference materials were

255   analysed twice, before and thereafter, 15 to 20 analyses (~every 1.5 hours) as well as at the

256   beginning and end of a run. Backgrounds were analysed for 30-seconds before the signal

257   from the ablated sample was acquired for 40-60 seconds. The laser was operated with ~3.5

258   J/cm^2 laser fluence and 5 Hz laser repetition rate. Samples were ablated in a He atmosphere

259   flowing at a rate of 0.8 l/min, followed by mixing of the ablation stream with the Ar carrier

260   gas (0.85 l/min) for introduction to the ICPMS.

261

262   The ICP-MS instrument was optimized to maximize sensitivity on mid- to high-mass

263   isotopes (>80 amu). Production of molecular oxide species (monitored as $^{232}Th^{16}O^+/^{232}Th^+$)

264   and doubly charged ion species (monitored as $^{140}Ce^{++}/^{140}Ce^+$) were maintained at levels

265   below 0.2%. Dwell times on each mass varied between 5 and 30 msec, depending on the

266   count rates. Total sweep time (time required to measure all isotopes once) was 0.76 sec. A

267   total of ~10 spot analyses, with spot size ranging from 15-35 μm, of sedimentary pyrites were

268   performed on each sample The pyrite (PPP-1) standard was analysed with same spot as

269   unknowns in order to account for Fe-S fractionation during ablation (Gilbert et al., 2014).

270   The glass standards were analysed with 51 μm spot size in order to alleviate heterogeneity of

271   the standards for key elements such as Au and Tl. Also, 5 spot analyses of the black shale

272   matrix (material surrounding the pyrites) were carried out on each sample to measure

273   concentrations of chalcophile and lithophile elements in siliciclastic matrix of the black

274   shales. Approximately, 10-12 analyses were performed on fine grained sedimentary pyrite

275   grains, containing abundant matrix inclusions, hence producing mixed analyses. Therefore, it

276   was necessary to deconvolute the analyses and extract the composition of clean pyrite. Both

277   matrix and pyrite analyses were used in the data reduction process in order to account for

278   mixing of pyrite and matrix components during LA-ICP-MS analyses of small pyrite grains.

279   The analyses of samples from the Velkerri and Wollogorang formations were processed by

280   an algorithm based on subtraction of the matrix component estimated from mass balance

281   (Large et al. 2014). The disadvantages of this method were subjectivity in selection of the

282   pyrite and matrix compositions and difficulty in determining uncertainties. The samples from

283   the Barney Creek Formation were reduced by the method of linear regression followed by

284   normalization of the total, which is described below. Uncertainties on analyses processed

285   using the regression method are presented in Appendix 2.   The analysis of a number of

286   samples from the Barney Creek were processed by both methods and produced consistent

287   results within 10% (Appendix 3).

288

289   The LA-ICP-MS analyses of pyrite from the Barney Creek formation were processed by an

290   Excel based data reduction software developed in-house, which uses a linear regression based

291   algorithm for determining chalcophile and siderophile abundances relative to sulphur, for

292   calculation of sulfide composition The conversion of raw data (counts per second) into

293   concentrations in ppm involved splitting the integration curve obtained from counts per

294   second vs analysis time, into five segments of equal duration. Concentrations represented by

295   each of these segments were reduced using time-equivalent portions of the signal obtained for

296   each of the calibration materials. The data in counts per second were then converted to

297   preliminary ppm values according to established methods (Longerich et al., 1996; Norman et

298   al. 1996), using Fe as the internal standard element. The method assumes a stoichiometric Fe

299   content of pyrite for calculating preliminary compositions, which are then normalized to a

300   100% total of all measured elements with the exception of C and Hg. To calculate the final

301   concentrations, a linear regression equation using S content was employed such that the sum

302   of the chalcophile elements is 100%. Regression fits for individual analyses were visually

303   inspected for all samples. The resulting compositions were close (Appendix 2) to major

304   element composition of stoichiometric pyrite. The analytical precision was estimated using

305   regression analysis for estimation of uncertainty on prediction, however ignoring

306   uncertainties on the measurements. For Se, As, Sb, Ni, Zn, Cu, Pb and Co at high

307   concentrations, the 90% relative uncertainty is <20% for the majority of the analyses.

308   However, uncertainty increases at lower concentrations. The relative analytical precision of

309   the replicate analyses of the standards was less than 5% Considering that concentrations of

310   many elements vary by 2-3 orders of magnitude in different samples, we conclude the

311   observed trends are outside of analytical uncertainty.

312

313   Sedimentary pyrites from the three black shale units were analysed for Co, Ni, Cu, Zn, As,

314   Se, Mo, Tl, Pb, Bi concentrations using the LA-ICP-MS (Table A2 a, b, c in Appendix 2). A

315   total of 29 black shale samples were selected for the study (Wollogorang Formation: 5;

316   Barney Creek Formation: 15; Velkerri Formation: 9) and ~ten pyrite spot analyses were

317   performed on each sample.

318

319   The pyrite data from the two formations i.e., Velkerri and Barney Creek have been published

320   in Mukherjee and Large (2016) and Mukherjee and Large (2017) respectively. Pyrite data

321   form the Wollogorang formation have been recently published in Mukherjee et al (2018)

322   along with other global Proterozoic formations in a large database provided as background

323   information in the Supplementary Information section of that paper. Here we provide the data

324   for the three formations again as it is the subject of detailed statistical treatment, discussion

325   and interpretation in the context of the McArthur Basin specifically.

326

327   **SHRIMP sulphur isotopes**

328

329   Sulphur isotope compositions (δ^{34}S and Δ^{33}S) of the pyrites were measured *in-situ* with the

330   SHRIMP-SI ion microprobe at the Research School of Earth Sciences, The Australian

331   National University (ANU). The same mounts used for laser ablation analysis were used for

332   SHRIMP analysis, in some cases the same grains Mounts were cleaned using ethanol, a dilute

333   alkaline cleaning solution, de-ionised water and dried in a vaccum oven at 60 °C for 24h.

334   Mounts were then coated with a film of ca. 40 nm of Au before pumping down in the sample

335   lock overnight. SHRIMP-SI measurements were performed with a Cs^+ primary beam of ~ 2

336   nA focused to sputter an area of ~ 25 μm in diameter. The sample mount was held at -10 kV

337   resulting in a final impact energy at the target of 15keV. Analytical conditions of the analyses

338   are similar to those described in Ireland et al. (2014). Faraday cups were used for

339   simultaneous detection of $^{32}S^-$, $^{33}S^-$, and $^{34}S^-$. $^{32}S^-$ was collected on a 10^{11} Ω resistor (50V

340   range), $^{33}S^-$ and $^{34}S^-$ on 10^{11} Ω resistors (5V range). Under the operating conditions used for

341   these analyses, typical count rates on $^{32}S^-$ were $\sim 0.2 - 1.2 \times 10^9$ cps, on $^{33}S^-$ about $1.2 - 9.2$

342     $\times 10^6$ cps, and on $^{34}S^-$ about $0.7 - 5.2 \times 10^7$ cps. Data collection consisted of 1 or 2 sets of 6-

343   10 subsets, 20 s each, with each subset comprising ten 2 s integrations.

344   Analyses of unknown pyrites were bracketed by measurements of pyrite reference material

345   Balmat ($\delta^{34}S = +15.1 \pm 0.2$‰, Crowe and Vaughan, 1996). The $^{33}S/^{32}S$ and $^{34}S/^{32}S$ ratios,

346   corrected for instrumental mass fractionation, are expressed here in standard delta notation in

347   permil (‰) relative to V-CDT (VCDT: Vienna-Canyon Diablo Troilite) scale, with

$$\delta^{33}S_{V-CDT} = 1000 \times \left[\frac{(^{33}S/^{32}S)_{corrected}}{(^{33}S/^{32}S)_{reference}} - 1 \right] (‰)$$

$$\delta^{34}S_{V-CDT} = 1000 \times \left[\frac{(^{34}S/^{32}S)_{corrected}}{(^{34}S/^{32}S)_{reference}} - 1 \right] (‰)$$

348   Capital delta values ($\Delta^{33}S$) have been calculated following Farquhar et al. (2003), where

$$\Delta^{33}S = \delta^{33}S - 1000 \times \left(\left(1 + \frac{\delta^{34}S}{1000} \right)^{0.515} - 1 \right)$$

349   Internal precision of single spot analyses of $\square^{34}S$ and $\Delta^{33}S$ are usually better than 0.08‰ and

350   0.3‰ (2SE; SE = standard error), respectively. External reproducibility of $\square^{34}S$ and $\Delta^{33}S$

351   values, calculated as the 1sigma standard deviation (SD) of all analyses on the Balmat

352   reference material over the course of an analytical session, were between 0.2 and 0.3‰.

353

354   **RESULTS**

355

356   **Pyrite Textures**

357

358   Only pyrite with framboidal textures, aggregates of fine-grained pyrite, or layers of fine-

359   grained pyrite, identified using reflected light microscopy, were selected for LA-ICP-MS and

360   SHRIMP-SI analyses as these are interpreted as primary diagenetic pyrite (Fig A1 in

361   Appendix 1). Pyrites from all three formations exhibited similar textures i.e., fine-grained

362   pyrite aggregates (10-100 μm) with the size of individual crystals varying between 5-10 μm.

363   However, at two intervals in the Wollogorang Formation intersection (65.8 m and 82.8 m),

364   the pyrites were coarser grained and possibly of hydrothermal origin. These grains were

365   excluded from this study because recrystallized and hydrothermal pyrites are known to have

366   different trace element concentrations and therefore would not reflect contemporaneous

367   seawater trace element chemistry (Large et al., 2009; Large et al., 2014; Gregory et al.,

368   2015a; Mukherjee et al., 2017). For instance, both coarse grained and fine grained pyrites

369   analyses in the same laser mount in the Barney Creek Formation yielded different trace

370   element concentrations (Fig A2 in Appendix 1)

371

372   **LA-ICP-MS pyrite trace element and matrix analyses**

373

374   Geometric means of individual sample intervals from all three formations are presented in

375   Table 1. Geometric means were calculated because trace element analyses in pyrite tend to

376   approximate log-normal distributions. Multiplicative standard deviations (MSD) of trace

377   elements are presented in Table 2. For all the elements presented, MSD ranges between 1 and

378   3. Mean (geometric) pyrite trace element concentrations of the entire set of analyses in the

379   three black shale units are also compared in Table 3.

380

381   Copper, Co, Tl and Bi show marked decreases in concentrations upsection from the

382   Wollogorang Formation to the Upper Velkerri Formation (Fig 4). Mean Co concentrations

383   decrease from 457 ppm in the Wollogorang Formation to 48 ppm in the Upper Velkerri

384   Formation (~9-fold decrease), while Cu decreases from 377 ppm in the Wollogorang

385   Formation to ~81 ppm in the Upper Velkerri Formation (~5-fold decrease). Molybdenum

386   shows a gradual decrease in concentration with higher concentrations in the Wollogorang (77

387   ppm) and Barney Creek Formations (79 ppm) compared to the Upper Velkerri Formation (20

388   ppm). Thallium shows a gradual decrease up stratigraphy with mean values decreasing from

389   20 to 5 ppm. On the other hand, concentrations of Zn and Se increase up stratigraphy (Fig 4).

390   The Zn mean increases from 28 ppm to 96 ppm, almost 3 times, whereas the Se mean

391   increases from 9 ppm to 19 ppm, only 2 times. Nickel, As, Ag and Pb show no obvious

392   trends with stratigraphy (Fig 4).

393

394   Trace element ratios Se/Co, Se/Bi, Ni/Co, Ni/Bi, Zn/Co, Zn/Bi and Mo/Co for the three

395   formations all increase upsection from the Wollogorang Formation to the Velkerri Formation,

396   with Mo/Bi remaining roughly constant (varying little between 6-13) in all three formations

397   (Fig 4). Downhole plots of Se, Mo, Co, Se/Co and Mo/Co for all three formations (Fig 5) also

398   indicate that [Se], Se/Co and Mo/Co increase, and Co and Mo decrease, upsection. The down

399   hole trends are compared with global mean values obtained from analyses of ~5000 pyrites

400   by Large et al. (2014, 2015a, b), as denoted by the black dashed line in Fig 5.

401

402   Statistical T tests were performed on the dataset to confirm that the differences in the

403   geometric mean concentration of TEs of the three formations are significant (Table 4). Mean

404   Mo, Se, Zn, Co, Bi concentrations of the Velkerri Formation are statistically significantly

405   different from those of the Wollogorang and Barney Creek Formations. Mean concentrations

406   of Co and Bi differ significantly between the Barney Creek Formation and Wollogorang

407   Formation, with no significant differences in the means of Mo, Se and Zn concentrations. The

408   mean Ni concentrations of all three black shales do not differ significantly. Other statistical

409   tests such as Spearman Correlations and Analyses of Variance (AOVs) confirm the T-test

410   results (See A1.3 in Appendix 1 and AOVs in Appendix 5).

411

412   Black shale matrix analyses for Ti, Zr, Th and Cr for evaluation of provenance, are presented

413   in Table 5. The mean Ti/Zr of the Velkerri, Barney Creek, and Wollogorang Formations are

414   22, 37 and 25 respectively. The Th/Cr ratios of Velkerri and Barney Creek Formations are ~1

415   and are slightly lower in the Wollogorang Formation (~0.40). Statistical treatment of the data

416   on matrix elements confirm no significant differences between the means of Ti/Zr and Th/Cr

417   ratios in the three black shale formations (Refer Appendix 6).

418

419   **SHRIMP-SI pyrite sulphur isotopes analyses**

420

421   A total of 124 sedimentary pyrite spot analyses were obtained for the three black shale

422   formations (Wollogorang Formation: 31; Barney Creek Formation: 31; Velkerri Formation:

423   62) (Table 6). The $\delta^{34}S_{VCDT}$ values of the pyrites from the Wollogorang Formation range

424   between -29.4 to +9.5‰ with an average of -5.03 ± 13.62‰ (n = 31; 1SD) (Table 6). Pyrites

425   from the Barney Creek Formation have a wider range of $\delta^{34}S_{VCDT}$ (-13.8 to +41.8‰) with an

426   average of +19.88 ± 17.7‰ (n = 31; 1SD) (Table 6). The $\delta^{34}S_{VCDT}$ values of pyrites from the

427   Velkerri Formation range from -14.2 to +65.6‰ with an average of +26.9 ± 16.5‰ (n = 62;

428   1SD), slightly higher than pyrites from the Barney Creek Fm. (Table 6). The Δ^{33}S values of

429   pyrites from all three formations are low, with values close to zero and an average of 0.36 ±

430   0.51‰ (n = 31; 1SD), 0.08 ± 0.28‰ (n = 31; 1SD) , and 0.01 ± 0.18‰ (n = 62; 1SD) for the

431   Wollogorang, Barney Creek, and Velkerri Formations, respectively (Table 6).

432

433   **DISCUSSION**

434
435   **Factors controlling trace element concentrations in pyrite**

436

437   The trace element composition of primary marine pyrite is considered to be a reflection of the

438   coexisting seawater at the time the pyrite formed (Large et al., 2014; 2015). The trace

439   element composition of sea water, in turn, is a function of the coeval sources and sinks, and

440   the residence time of the element in seawater. The latter depends critically on the speciation

441   of the element in the ocean under ambient conditions at any given time. This study takes into

442   account the geological factors: oxidative weathering, tectonic setting and composition of

443   source rocks as determinants of the TE source flux. Whereas factors such as areal extent and

444   types of sinks (oxic, sub-oxic, anoxic) and residence time, likely determine the sink flux. Our

445   main focus in this paper is to evaluate whether trace element concentrations in diagenetic

446   pyrites were a function of changes in source fluxes or changes in areal extent of sinks, or

447   both, i.e., to evaluate possible causes for the trace element compositional variations measured

448   in sedimentary pyrites of the three formations.

449

450   *Oxidative weathering*

451

452   Oxidative weathering on the continents results in the release of redox sensitive trace elements

453   to solution. Trace elements are then transported by rivers to continental margins where they

454   are either sequestered into estuaries or continental margin sediments, or transported to

455   seawater etc. Once in the open ocean, they can be sequestered into pelagic sediments by

456   reduction upon encountering a redox boundary in the water column or sediment-water

457   interface where they may form complexes with organic acids and become incorporated into

458   authigenic sulphides.

459

460   Trace elements such as Mo, Zn, Se, Co, Ni, Cu, As are known to be redox-sensitive, (i.e., will

461   generally undergo a change in mobility at oxidizing or reducing geochemical barriers) and

462   are known to respond to changes in atmosphere-ocean redox conditions (Calvert and

463   Pedersen, 1993; Jones and Manning, 1994; Wignall, 1994; Crusius et al., 1996; Dean et al.,

464   1997, 1999; Yarincik et al., 2000; Morford et al., 2001; Pailler et al., 2002; Algeo and

465   Maynard, 2004; Algeo et al., 2009; 2012; Tribovillard et al., 2006; Nishri and Halicz, 2014;

466   Smith and Huyck, 1999) Table 7. While some elements are not redox-sensitive sensu stricto

467   (Bi, Pb), their speciation in the water column is controlled by redox conditions of the

468   atmosphere-ocean system (Refer Table 7). Not all redox sensitive elements in pyrite can be

469   used to infer atmospheric redox conditions because of partitioning into different phases

470   (organic, detrital) other than pyrite. For instance, Ni and Cu may be adsorbed onto organic

471   complexes and Fe-Mn oxides/hydroxides in the sedimentary process. Silver and Tl are not

472   redox sensitive, however Tl in pyrite can be used to screen out pyrites affected by

473   hydrothermal events (Large et al., 2009; Mukherjee and Large, 2016). Some redox sensitive

474   elements (Pb, As) in pyrites may not record any oxygenation trend solely due to their

475   abundant supply in the water column (high source flux). Arsenic is particularly problematic

476 due it being relatively more mobile under reducing conditions than other redox sensitive TE

477 (Smedley and Kinniburgh, 2002).

478

479 An increase in concentrations of redox sensitive elements Se and Zn from ~1730 Ma to 1360

480 Ma suggests an increased supply of these elements into the water column via oxidative

481 weathering on land. Decreases in concentrations of Co and Bi can also be used to support the

482 hypothesis that these elements may have been retained, relatively more than other elements,

483 by Fe-Mn hydroxides and oxides, an important product of oxidative weathering on land. The

484 premise on which the hypothesis is based is described below.

485

486 Experiments have shown that Fe, Al and Mn hydroxides and oxides, and particularly

487 manganese oxides (Gadde and Laitinen, 1974) are efficient scavengers of trace elements in

488 their cationic form (Jackson, 1998; Huang and Germida, 2002; Sparks, 2003; Violante et al.,

489 2008). It is also known that manganese oxide has a special preference for Co compared to

490 other elements in their cationic/anionic form (Smith, 1999). Further evidence lies in

491 experiments designed to understand interactions of certain elements with manganese

492 hydrooxides/oxides (Murray et al., 1968, 1975) where the elements showed affinity in the

493 following order $Mg < Ca < Sr < Ba < Ni < Zn < Mn <-Co$. Furthermore, manganese oxides

494 specifically, α-Mn_2O_3, is known to adsorb cobalt much more than Ni, Zn or Cu, according to

495 experiments by McKenzie (1972). Therefore it is possible that the supply of cobalt to the

496 ocean is inhibited by oxidative processes on land where it is retained by oxides/hydroxides on

497 land. (Pickering, 1979; Jackson, 1998; Huang and Germida, 2002; Sparks, 2003; Violante et

498 al., 2008).

499

500   Another evidence supporting this hypothesis comes from three different lines of research on

501   Co concentrations though time. Thermodynamic modelling of the concentration of Co in the

502   oceans (Zerkle et al., 2005), Co concentrations in sedimentary pyrite (Large et al., 2014) and

503   Co/Ti in iron formations (Swanner et al., 2014) collectively confirm that Co concentrations in

504   the oceans have decreased through time coinciding with increases in atmospheric pO_2. Where

505   elements like Se and Mo have shown an increase through time in response to oxygenation,

506   Co shows a reverse trend (Large et al., 2014

507

508   Bismuth behaves similar to Co (despite not being strictly redox sensitive) in response to

509   increases in oxygenation. The element Bi enters the marine realm via two main sources;

510   atmospheric inputs i.e., eolian dust of volcanic origin (Lee et al., 1985; 1986) or river influx,

511   both being comparable source materials of Bi (Bertine et al., 1996). Bismuth, owing to its

512   extensive hydrolytic activity and strong particle reactivity, is also retained in oxyhydroxides,

513   particularly manganese phases (Barnes, 1967; Fowler et al., 2010), resulting in very low

514   concentrations of Bi in modern sea water (Bertine et al., 1996). Currently there is no

515   thermodynamically modelled trend for Bi in the oceans through time. Nevertheless, Large et

516   al. (2014) pointed out that Bi was one of the least abundant trace elements in the ocean today,

517   with a very short residence time (in the order of 20 years; Bertine et al.), 1996 and, like Co,

518   possibly decreased in concentration in pyrite as it was retained by Mn-oxides forming in

519   response to oxidative weathering on land.

520

521   Surprisingly, our data shows that Mo concentrations in pyrite decreased from 1730 Ma to

522   1360 Ma. This is surprising because Mo concentration in shales has been used to track redox

523   changes in the ocean and atmosphere (Scott et al., 2008; Gordon et al., 2008; Kendall et al.,

524   2009; Sahoo et al., 2012) and, whereas most other trace element data indicates an increase in

525   oxygenation of the atmosphere, the Mo concentrations measured in the pyrites studied here

526   seem to suggest a decrease in atmospheric oxygen over this period. It is possible that Mo is

527   retained in the black shale matrix rather than pyrite, causing the values in pyrite to be

528   suppressed in the (~1360 Ma) Velkerri Formation. However, that is not the case for our data.

529   Whole rock values of Mo in the Velkerri Formation have previously been compared to their

530   concentration in pyrite by Mukherjee et al., (2016). Whole rock Mo concentrations range

531   between 2-37 ppm compared to 4-795 ppm in pyrite. The other reason for this surprising

532   behavior of Mo could be a source flux issue i.e., a possibly Mo-rich source for the Tawallah

533   Group. The possibility that Mo could be weathered and mobilized even under mildly oxic

534   weathering conditions (Anbar et al., 2007) and is very sensitive to sulphide oxidation

535   (William and Rickaby, 2012) could also potentially lead to Mo-rich pyrites of the

536   Wollogorang Formation.

537

538   This unusual decrease in Mo in pyrite suggests caution when using a single particular trace

539   element concentration or isotope ratio as a proxy for tracking changes in redox conditions.

540   Another way of tackling this issue is to use ratios of two elements that exhibit antithetic

541   behavior i.e., one element that might be expected to increase in concentration in pyrite with

542   atmosphere oxidation, and the other that might be expected to decrease in concentration in

543   pyrite. Thus, a more robust way to evaluate atmosphere oxygenation would be to couple

544   certain trace elements that show enrichments in pyrite under conditions of increasing

545   oxygenation (e.g., Se, Zn, Mo, Ni) with others that show depletions in pyrite under conditions

546   of increasing oxygenation (e.g., Co, Bi). For instance, even though pyrite from the

547   Wollogorang Formation shows increased Mo concentrations relative to pyrite from the

548   Velkerri shales, the higher Co and Bi contents of pyrite argue against the possibility of

549   oxygenation Similarly, Ni in pyrite does not display a particular trend, but its concentration

550   increases with respect to Co at any given time through the 370-million-year period. All of the

551   Co/Bi ratios (Ni/Co, Se/Co, Mo/Co, Zn/Co and Zn/Bi ratios in Fig 6; Table 3) increase with

552   sedimentation age and provide robust evidence for increasing atmosphere oxygenation over

553   this interval of time (1730 to 1360 Ma).

554

555   *Source rock composition*

556

557   So far, our discussion of redox-sensitive trace element compositions in pyrite in the

558   Proterozoic marine sediments studied here has been linked to an increase in atmospheric

559   oxygen, which is assumed to be related directly to the intensity of oxidative weathering on

560   the continents. Nevertheless, source rock compositions (dominantly mafic or felsic) and basin

561   tectonics (active or less active) at the time of deposition of these black shales, are important

562   factors that need to be addressed in order to evaluate the nature of the trace element flux.

563   Below we summarise previous work on provenance analyses of the three black shale

564   formations studied here. Past studies of their sedimentology, including paleo current

565   measurements, sequence stratigraphy, and U-Pb zircon geochronology, have indicated that

566   the Wollogorang and Barney Formation sediments were derived from weathering and erosion

567   of the basal Tawallah Group, i.e., local sources. Deposition of these formations was related to

568   stretching and thinning of the basin floor in a rift environment (Rogers, 1996; Giles et al.,

569   2002). On the other hand, the Roper Group was deposited in an intracratonic ramp setting

570   soon after the Isan Orogeny (Abbott and Sweet, 2000). Sediments of the Roper Group are

571   likely to have been derived from the weathering and erosion of the North Australian craton

572   basement rocks (Munsen et al., (2016). The question of whether the characteristic pyrite trace

573   element concentrations in the Velkerri Formation have been affected due to change in

574   provenance, needed to be further investigated.

575

576   We used Ti, Zr, Th, and Cr concentrations, augmented by literature data, to investigate

577   potential influences of source rock composition on trace element concentrations in pyrite.

578   Several studies have highlighted the importance of trace element ratios (Cr/Ni, V/Cr, V/Ni,

579   La/Yb, La/Sm, Ti/Zr, Y/Ni, Zr/Cr, etc.) in determining the type of source rocks from which

580   the sediments were derived (Bhatia, 1983; Condie and Wronkiewicz, 1990; McLennan et al.,

581   1990; McLennan and Taylor, 1991; Garver and Scott, 1995; Cingolani et al., 2003; Ali et al.,

582   2014). We have taken a similar approach and used Ti/Zr and Th/Cr ratios of the matrix to

583   infer differences in the types of source rocks (Table 5; black shale matrix analyses of Ti, Zr,

584   Cr, Th). This approach is based on the premise that Ti and Cr are more enriched in mafic

585   rocks (means 10,000 and 250 ppm respectively; Riemann and De Caritat, 1998) than felsic

586   rocks (means 3,000 and 10 ppm respectively), while Zr and Th are enriched in felsic rocks

587   (means of 200 and 15 ppm respectively) relative to basic rocks (means 120 and 2.2 ppm).

588   Figure 7 illustrates these compositions in a plot between Ti/Zr and Th/Cr with an assigned

589   point for mean basalt and rhyolite. It is evident from Fig 7 (Th/Cr and Ti/Zr ratios of

590   analyses) that all three black shale formations cluster together near the rhyolite (felsic) mean

591   rather than showing any consistent variable association. In all three cases, source rocks are

592   interpreted to be similar in terms of composition. The formation that most deviates from a

593   rhyolitic source towards a mafic source is the Velkerri Formation which is depleted in Co,

594   which would be expected to be enriched if the source of the trace elements was largely

595   detrital. The data suggests that changes in trace element concentrations in the pyrites are most

596   likely related to changes in the redox state of the atmosphere rather than changes in source

597   rock compositions available for erosion.

598

599   We have considered only the source flux of the trace elements in the above discussion.

600   However, changes in sink fluxes could be important in controlling trace element

601   concentrations in pyrite, as a result we have used sulphur isotope compositions of pyrite to

602   give us an insight into changes in sinks, described in the next section.

603

604   **Sulphur isotopes in the McArthur Basin**

605

606   Sulphur isotope compositions of sedimentary sulphides and sulphates of the McArthur Basin

607   sediments have been studied by a number of researchers (Donnelly and Jackson, 1988;

608   Canfield, 1998; Shen et al., 2002; Shen et al., 2003; Kah et al., 2004; Lyons et al., 2006;

609   Johnston et al., 2008). All three black shale units have been sampled for sulphur isotope

610   analysis in order to understand the amount and patterns of fractionation between sea water

611   sulphate and sulphide, including constraining sea water sulphate levels in the Middle

612   Proterozoic (Canfield, 1998). The previous studies (using measured values of $\delta^{34}S_{CAS-PY}$ and

613    $\partial\delta^{34}S_{CAS}/\partial t_{(max)}$; CAS: Carbonate-associated sulphate and PY: pyrite) indicate that the Middle

614   Proterozoic was a period of very low sea water sulphate values (0.1-1.8mM) compared to

615   28mM today (Kah et al., 2004; Luo et al., 2015). Based on S-isotope patterns, it has also been

616   suggested that the Wollogorang and Velkerri Formations were deposited in a basin connected

617   to the global ocean (Shen et al., 2002; Shen et al., 2003; Johnston et al., 2008). The Barney

618   Creek Formation, on the other hand, has features that suggest it formed in a semi-restricted

619   basinal environment with progressive interaction with the global sulphate reservoir during its

620   deposition (Johnston et al., 2008).

621

622   As part of this study, sedimentary pyrite was analysed for ^{32}S-^{33}S-^{34}S, in order to understand

623   variations of $\delta^{34}S$ in pyrite between the three black shales. $\delta^{34}S_{VCDT}$ in the Velkerri Formation

624   displays the greatest range and the highest mean of all three formations (-14.2 to +52.8‰;

625   mean: +26‰) (Fig 8; Table 7). The Barney Creek Formation has a similar range of $\delta^{34}S_{VCDT}$

626   values but a lower mean (-13.8 to +41.8‰; mean: +19.5‰), (Fig 8). In contrast, the

627   Wollogorang Formation has a more restricted range of $\delta^{34}S_{VCDT}$, extending to the most

628   negative values observed in this study, and the lowest mean (-29.4 to +9.5‰; mean: -5.0‰)

629   (Fig 8).

630

631   The in-situ $\delta^{34}S$ values in pyrite obtained using SHRIMP-SI had a similar range and mean

632   when compared to the conventional techniques utilized in previous research (Johnston et al.,

633   2008; Shen et al., 2002). This is indicated in Figure 8 where the shaded regions represent the

634   range of data obtained by previous studies. However, in some instances our data show a

635   greater spread compared with other studies. This is to be expected when results of a micro-

636   beam technique are compared with those of a micro-drill technique. We have documented

637   extremely heavy pyrites (^{34}S enriched) in the Barney Creek and Velkerri Formations relative

638   to published data. Based on the $\delta^{34}S$ values presented in Tables 6, all three formations also

639   have negative $\delta^{34}S$ values, which could be indicative of microbial activity i.e., bacterial

640   sulphate reduction. Pyrite from the Wollogorang Formation records the most negative $\delta^{34}S$

641   values (-20 to -30‰) relative to the other two formations where the negative $\delta^{34}S$ values

642   range between 0 to -14‰ (see above quoted data). Similarly, pyrite in the Wollogorang

643   Formation has the least positive $\delta^{34}S$ values (maximum of +10‰), compared to >40‰ in the

644   Barney Creek Formation >50‰ in the Velkerri Formation. Overall, there is an increase in not

645   only the range of positive $\delta^{34}S$ values but also the $\delta^{34}S$ mean of each formation up

646   stratigraphy (Table 6).

647

648   This increasing trend of $\delta^{34}S_{pyrite}$ values upsection could be interpreted in several ways.

649   Negative $\delta^{34}S$ values are generally interpreted as being associated with microbial sulphate

650   reduction because of the preferential uptake of ^{32}S relative to ^{34}S in sulphide, as the process is

651   chemically and kinetically more favourable in metabolic pathways. This causes low values of

652    $\delta^{34}S_{pyrite}$ and can be reflected in later diagenetic pyrite that forms from the ^{34}S-depleted pore

653   fluids. Thus, any increase in $\delta^{34}S_{pyrite}$, is difficult to attribute to microbial activity acting on an

654   effectively infinite reservoir of sulphate. However, diagenetic pyrite could either be more

655   depleted or more enriched in ^{34}S depending on whether it precipitates in an open or close

656   system, which regulates the supply of sulphate in the area of pyrite formation.

657

658   Generally, heavy pyrites (^{34}S enriched) are attributed to precipitation under a closed system

659   (with limited or no additional supply of sulphate) (Shen et al., 2002; Shen et al., 2003;

660   Johnston et al., 2008; Gregory et al., 2015b). Continuing sulphate reduction leads to

661   progressively ^{34}S-enriched pyrites as they begin to record the isotopic signature of the closed-

662   system sulphate. If that were the case, the data from the present study would indicate that the

663   increasing trend of $\delta^{34}S$ values upsection reflects a transition from an open system in the

664   Wollogorang Formation to a closed system in the Velkerri Formation. However, such a

665   scenario is not compatible with sedimentological, paleontological and geochemical studies

666   that have confirmed an open marine origin for these rocks (Jackson et al., 1991; Abbott and

667   Sweet, 2000; Shen et al., 2003; Javaux et al., 2001; Kendall et al., 2009). Previous studies

668   have attributed the negative $\delta^{34}S$ values in the Velkerri Formation to reduction of sea water

669   sulphate in a basinal setting with non-limiting sulphate supply and vice versa. (Logan et al.,

670   1995; Shen et al., 2003). Johnston et al. (2008) used not only $\delta^{34}S_{pyrite}$ but ^{33}S and ^{36}S (larger

671   variability in $\Delta^{33}S$ inversely correlated to $\Delta^{36}S$) to show that pyrite deposition in the Velkerri

672   Formation black shales occurred in an open marine setting with connectivity to the global

673   ocean. In fact, Kah et al. (2004) and Luo et al. (2015) proposed an increase in sea water

674   sulphate levels based on their measured values of sulphur isotopes in the pyrites from the

675   Velkerri Formation.

676

677   The Barney Creek Formation is considered to have formed in a partly restricted basin, and

678   the positive $\delta^{34}S_{pyrite}$ values may be related to the closed system behavior. Indeed, previous

679   studies by Shen et al. (2002) and Johnston et al. (2008) have pointed out that the limited

680   supply of sulphate in a closed system may have rendered $\delta^{34}S$ values in pyrite close to

681   contemporaneous sea water (+25‰). However, we observe much heavier values than

682   reported in the literature so far. Closed system behavior could also be created locally within

683   sediments below the sediment-water interface. That could have led to a tendency toward

684   heavy values in the Barney Creek and Velkerri Formations, but interestingly, very heavy

685   values are absent from the Wollogorang Formation. Therefore, it is not possible to link the

686   increasing trend of $\delta^{34}S$ values we observe in our pyrite to microbial sulphate reduction, lack

687   of connection to global ocean, or quantitative sulphate reduction in the sediments. The

688   increasing trend of $\delta^{34}S$ values upsection demands an alternative explanation, which we

689   explore below.

690

691   We suggest an alternative explanation for the increasing mean $\delta^{34}S$ trend with the help of a

692   simple schematic diagram (Fig 9). Two scenarios are proposed; scenario 1 represents

693   depositional conditions of the Wollogorang Formation, and scenario 2 represents the

694   depositional conditions of the Velkerri Formation. The Barney Creek depositional condition

695   is assumed to be intermediate between these two scenarios. Both scenarios represent open

696   marine conditions with low global sulphate levels in the oceans, as is the case with the three

697   black shale formations. In scenario 1, there is less oxygen in the atmosphere impeding

698   oxidative weathering on land. This leads to a low supply of certain trace elements, sulphate

699   and other nutrients that, in turn, would cause low productivity and possibly growth of the

700   prevalent biologic community at 1730 Ma, and consequent lower organic matter production

701   and deposition. In this case, it is envisaged that black shales are forming in an anoxic

702   environment mainly due to low organic matter deposition and a lack of oxygen in the water

703   column related to low pO_2 in the atmosphere. Low productivity would cause a decrease in the

704   availability of reactive organic compounds for sulphate reduction. Scenario 1 reflects anoxic

705   conditions over a large area of the ocean floor, with lower sulphate reduction rates & lower

706   pyrite burial proportions, and consequently forming pyrites that lack heavy $\delta^{34}S_{pyrite}$ values.

707

708   Scenario 2 has higher oxygen contents in the atmosphere, causing greater oxidative

709   weathering on land. This leads to a higher input of trace elements, sulphate and nutrients in

710   the ocean, promoting an increase in organic matter production and organic carbon deposition.

711   This causes two important changes. First, increased productivity, leads to increased release of

712   oxygen into the ocean and atmosphere, and second, higher levels of organic carbon

713   production and deposition ensures ample availability of reactive organic compounds in the

714   sediments for sulphate reduction. Subsequently, the process leads to a strongly reducing

715   environment (anoxic to euxinic) with higher sulphate reduction rates and pyrite burial

716   compared to scenario 1. The pockets or sub-basins of anoxia are believed to be more focused,

717   possibly due to basin architecture and also the increase in oxygen of the overall ocean-

718   atmosphere system, causing the region of anoxia/euxinia to shrink (organic matter is

719   regionally oxidized and only locally preserved in sub-basins). However, because organic

720   matter deposition occurs over a smaller area, it causes sulphate reduction rates and pyrite

721   burial to be higher. In turn, this causes a relative increase in $\delta^{34}S$ values in pyrite compared

722   with scenario 1 (Fike and Grotzinger, 2008, Leavitt et al., 2013; Fike et al., 2015; Pasquier et

723   al., 2017; Liu et al., 2019).

724

725   The proposed oxygenation event is also consistent with an ocean oxygenation event at ~1400

726   proposed by Yang et al. (2017) using U isotopes and the previously proposed increase in sea

727   water sulphate concentrations (Kah et al., 2004; Luo et al., 2015) due to oxidative weathering

728   on land. The observed increased complexity of microorganisms in the Velkerri Formation

729   relative to Barney Creek and Wollogorang Formations (Javaux et al., 2001; 2004), may also

730   be attributed to these changes. Although this model is qualitative, speculative and requires

731   further study to evaluate, it is supported by marine S isotope fractionation at another critical

732   time in ocean evolution. The increase of δ^{34}S values in pyrite during the Neoproterozoic

733   Oxygenation Event (NOE or GOE 2) is apparent at the Precambrian-Cambrian transition

734   (Claypool et al., 1980; Strauss and Schieber, 1990; Strauss et al., 1992; Strauss, 1993) where

735   δ^{34}S$_{pyrite}$ varies between +7.6 to +53‰ over the period 600 to 520 Ma, followed by the

736   Cambrian explosion of life. Although, a number of primary (Fike and Grotzinger, 2008; Ries

737   et al., 2009, Fike et al., 2015) and secondary (Cui et al., 2018) processes could explain the

738   phenomenon. Modern-day examples of isotopically heavy pyrites under the current high pO$_2$

739   are described in (Borowski et al., 2000; Borowski et al., 1996; Borowski et al., 2013;

740   Jãrgensen et al., 2004; Lin et al., 2016). In addition, strongly reducing environments, such as

741   those found in the Black Sea and Cariaco Basin, do not impart heavy values of δ^{34}S in pyrite

742   compared to Proterozoic black shales. This could be due to the vast reservoir of sea water

743   sulphate (28mM) today compared to the Proterozoic (0.1-1.8mM) [Luo et al., 2015].

744

745   **IMPLICATIONS**

746

747   Trace element concentrations (and their ratios) of sedimentary pyrite in three black shale

748   formations of the McArthur Basin provide evidence for a gradual increase in atmospheric

749   oxygenation from 1730 to 1360 Ma. We also observe a marked change in pyrite sulphur

750   isotopic compositions in the three black shale formations i.e., a marked increase in mean

751     $\delta^{34}S_{pyrite}$ values from the Wollogorang Formation to the Velkerri Formation. This is possibly

752   indicative of expansion of oxygenated waters and decreasing areal extent of anoxia. Results

753   from both techniques have major implications on the atmospheric redox evolution in "Boring

754   Billion", a period believed to witness non-fluctuating redox conditions.

755

764

765   **References**
766
767
768   Abbott, S.T., and Sweet, I.P. (2000) Tectonic control on third-order sequences in a
769   siliciclastic ramp-style basin: an example from the Roper Superbasin (Mesoproterozoic),
770   northern Australia. Australian Journal of Earth Sciences, 47, 637–657.

771   Ahmad, M., Dunster, J.N., and Munson, T.J. (2013) Chapter 15: McArthur Basin: in Ahmad,
772   M., and Munson, T.J. (compilers). 'Geology and mineral resources of the Northern
773   Territory'. Northern Territory Geological Survey, Special Publication 5.

774 Algeo, T.J., and Maynard, J.B. (2004) Trace element behavior and redox facies in core shales
775 of Upper Pennsylvanian Kansas-type cyclothems. Chemical Geology, 206, 289–318.

776 Algeo, T.J., and Lyons, T.W. (2006) Mo–total organic carbon covariation in modern anoxic
777 marine environments: Implications for analysis of paleoredox and paleohydrographic
778 conditions. Paleoceanography, 21, 1- 23.

779 Algeo, T.J., and Rowe, H. (2012) Paleoceanographic applications of trace-metal
780 concentration data. Chemical Geology, 324, 6–18.

781 Algeo, T.J., and Tribovillard, N. (2009) Environmental analysis of paleoceanographic
782 systems based on molybdenum-uranium covariation. Chemical Geology, 268, 211–225.

783 Ali, S., Stattegger, K., Garbe Schöngerg, D., Frank, M., Kraft, S., and Kuhnt, W. (2014) The
784 provenance of cretaceous to quaternary sediments in the Tarfaya basin, SW Morocco:
785 evidence from trace element geochemistry and radiogenic Nd-Sr isotopes. Journal of African
786 Earth Sciences, 90, 64–76.

787 Anbar, A.D., and Knoll, A.H. (2002) Proterozoic ocean chemistry and evolution: a
788 bioinorganic bridge? Science, 297, 1137–1142.

789 Anbar, A.D., Duan, Y., Lyons, T.W., Arnold, G.L., Kendall, B., Creaser, R.A., Kaufman,
790 A.J., Gordon, G.W., Scott, C., Garvin, J. and Buick, R. (2007) A whiff of oxygen before the
791 great oxidation event? Science, 317, 1903–1906.

792 Arnold, G.L., Anbar, A.D., Barling, J., and Lyons, T.W. (2004) Molybdenum isotope
793 evidence for widespread anoxia in Mid-Proterozoic ocean. Science, 304, 87-90.
794
795 Barnes, S.S. (1967) Minor element composition of ferromanganese nodules. Science, 157,
796 63-65.
797
798 Bertine, K.K., Koide, M. and Goldberg, E.D. (1996) Comparative marine chemistries of
799 some trivalent metals-bismuth, rhodium and rare Earth elements. Marine Chemistry, 53, 89–
800 100.
801
802 Bertine, K.K., and Turekian, K.K. (1973) Molybdenum in marine deposits. Geochimica et
803 Cosmochimica Acta, 37, 1415–1434.
804
805 Bhatia, M.R. (1983) Plate tectonics and geochemical composition of sandstones. Journal of
806 Geology, 91 (6), 611–627.

807 Borowski, W.S., Hoehler, T.M., Alperin, M.J., Rodriguez, N.M., Paull, C.K. (2000)
808 Significance of anaerobic methane oxidation in methane-rich sediments overlying the Blake
809 Ridge gas hydrates. In: Paull, C.K., Matsumoto, R., Wallace, P.J., Dillon, W.P. (Eds.),
810 Proceedings of the Ocean Drilling Program, Scientific Results, 87-99.

811 Borowski, W.S., Paull, C.K., Ussler, W. (1996) Marine pore-water sulfate profiles indicate in
812 situ methane flux from underlying gas hydrate. Geology, 24, 655-658.

813   Borowski, W.S., Rodriguez, N.M., Paull, C.K., Ussler III, W. (2013) Are 34S-enriched
814   authigenic sulfide minerals a proxy for elevated methane flux and gas hydrates in the
815   geologic record? Marine and Petroleum Geology, 43, 381-395.

816   Brasier, M.D., and Lindsay J.F. (1998) A billion years of environmental stability and the
817   emergence of eukaryotes: new data from northern Australia. Geology, 26, 555–558.

818   Brocks, J., Grosjean, E., and Logan, G. (2008) Assessing biomarker syngeneity using
819   branched alkanes with quaternary carbon (BAQCs) and other plastic contaminants.
820   Geochimica et Cosmochimica Acta, 72, 871-888.

821   Brocks, J.J., Love, G.D., Summons, R.E., Knoll, A.H., Logan, G.A., and Bowden, S.A.
822   (2005) Biomarker evidence for green and purple sulphur bacteria in a stratified
823   Paleoproterozoic sea. Nature, 437, 866-870.

824   Brookins, D.G. (1988) Bismuth. In: Eh-pH Diagrams for Geochemistry. Springer,
825   Heidelberg, Berlin.
826
827   Buick, R., Des Marais, D.J., and Knoll, A.H. (1995) Stable isotopic compositions of
828   carbonates from the Mesoproterozoic Bangemall group, northwestern Australia. Chemical
829   Geology, 123 (1–4), 153–171

830   Bull, S.W. (1998) Sedimentology of the Palaeoproterozoic Barney Creek Formation in DDH
831   BMR McArthur 2, Southern McArthur Basin, Northern Territory. Australian Journal of Earth
832   Sciences, 45, 21–23.

833   Calvert, S.E., and Pedersen, T.F. (1993) Geochemistry of Recent oxic and anoxic marine
834   sediments: implications for the geological record. Marine Geology, 113, 67– 88.
835
836   Canfield, D.E. (1998) A new model for Proterozoic ocean chemistry. Nature, 396, 450–453.

837   Chappaz, A., Lyons, T.W., Gregory, D.D., Reinhard, C.T., Gill, B.C., Li, C., and Large, R.R.
838   (2014) Does pyrite act as an important host for molybdenum in modern and ancient euxinic
839   sediments? Geochimica et Cosmochimica Acta, 126, 112–122.

840   Chen, J., Walter, M.R., Logan, G.A., Hinman, M.C., and Summons, R.E. (2003) The
841   Paleoproterozoic McArthur River (HYC) Pb/Zn/Ag deposit of northern Australia: organic
842   geochemistry and ore genesis. Earth and Planetary Science Letters, 210, 467-479.

843   Cingolani, C.A., Manassero, M., and Abre, P. (2003) Composition, provenance, and tectonic
844   setting of Ordovician siliciclastic rocks in the San Rafael block: Southern extension of the
845   Precordillera crustal fragment, Argentina. Journal of South American Earth Sciences, 16 (1):
846   91-106

847   Claypool, G.E., Holser, W.T., Kaplan, I.R., Sakai, H., and Zak, I. (1980) The age curves of
848   sulfur and oxygen isotopes in marine sulphate and their mutual interpretations. Chemical
849   Geology, 28, 199-260

850   Condie, K.C., and Wronkiewicz, D.S. (1990) The Ce/Th ratio of Precambrian pelites from
851   the Kaapvaal Craton as an index of cratonic evolution. Earth and Planetary Science Letters,

852   97, 256–267

853   Crick, I.H., Boreham, C.J., Cook, A.C., and Powell, T.G. (1988) Petroleum geology and
854   geochemistry of Middle Proterozoic McArthur Basin, northern Australia II: assessment of
855   source rock potential. American Association of Petroleum Geology Bulletin, 72, 1495–1514.

856   Crowe, D.E., and Vaughan, R.G. (1996) Characterization and use of isotopically
857   homogeneous standards for in situ laser microprobe analysis of 34S/32S ratios. American
858   Mineralogist, 81, 1987-193.

859   Crowe, S.A., Døssing, L.N., Beukes, N.J., Bau, M., Kruger, S.J., Frei, R., and Canfield, D.E.
860   (2013) Atmospheric oxygenation three billion years ago. Nature, 501, 535–538.

861   Crusius, J., Calvert, S., Pedersen, T., and Sage, D. (1996) Rhenium and molybdenum
862   enrichments in sediments as indicators of oxic, suboxic and sulfidic conditions of deposition.
863   Earth and Planetary Science Letters, 145, 65–78.
864
865   Cui, H., Kitajima, K., Spicuzza, M.J., Fournelle, J.H., Denny, A., Ishida, A., Zhang, F.,
866   Valley, J.W. (2018). Questioning the biogenicity of Neoproterozoic superheavy pyrite by
867   SIMS. American Mineralogist, 103, 1362-1400.

868   Danyushevsky, L., Robinson, P., Gilbert, S., Norman, M., Large, R., McGoldrick, P., and
869   Shelley, M. (2011) Routine quantitative multi-element analysis of sulphide minerals by laser
870   ablation ICP-MS: Standard development and consideration of matrix effects. Geochemistry:
871   Exploration, Environment, Analysis, 11, 51–60.

872   Dean, W.E., Gardner, J.V., and Piper, D.Z. (1997) Inorganic geochemical indicators of
873   glacial – interglacial changes in productivity and anoxia of the California continental margin.
874   Geochimica et Cosmochimica Acta, 61, 4507– 4518.
875
876   Dean, W.E., Piper, D.Z., and Peterson, L.C. (1999) Molybdenum accumulation in Cariaco
877   basin sediment over the past 24 k.y.: a record of water-column anoxia and climate. Geology,
878   27, 507– 510.
879
880   Donnelly, T.H., and Jackson, M.J. (1988) Sedimentology and geochemistry of a mid-
881   Proterozoic lacustrine unit from northern Australia. Sedimentary Geology, 58, 145–169.
882
883   Donnelly, T.H., and Crick, I.H. (1988) Depositional environment of the middle Proterozoic
884   Velkerri Formation in northern Australia: geochemical evidence. Precambrian Research, 42,
885   165–172.

886   Farquhar, J., and Wing, B.A. (2003) The terrestrial record of stable sulphur isotopes: a review
887   of the implications for evolution of Earth's sulphur cycle. Earth and Planetary Science
888   Letters, 213, 1–13.
889
890   Fike, D.A., and Grotzinger, J.P. (2008) A paired sulfate-pyrite δ34S approach to
891   understanding the evolution of the Ediacaran-Cambrian sulfur cycle. Geochimica et
892   Cosmochimica Acta, 72, 2636-2648.
893

894   Fike, D.A., Bradley, A.S., and Rose, C.V. (2015) Rethinking the ancient sulfur cycle. Annual
895   Review of Earth and Planetary Sciences, 43, 593-622.
896
897   Fowler, S.W., Teyssie, J.L., and Church, T.M. (2010) Scavenging and retention of bismuth
898   by marine plankton and biogenic particles. Limnology and Oceanography, 55, 1093–1104.

899   Gadde, R.R., and Laitinen, H.A., 1974. Heavy metal adsorption by hydrous iron and
900   manganese oxides. Analytical Chemistry, 46 (13), 2022–2026

901   Garver, J.I., and Scott, T.J. (1995) Trace elements in shale as indicators of crustal provenance
902   and terrane accretion in south Canadian Cordillera. Geological Society of America Bulletin,
903   107, 440–453

904   Gilbert, S., Danyushevsky, L., Goemann, K., and Death, D. (2014) Fractionation of sulphur
905   relative to iron during laser ablation-ICP-MS analyses of sulphide minerals: implications for
906   quantification. Journal of Analytical Atomic Spectrometry, 29, 1024–1033.

907   Giles, D., Betts, P.G., Lister, G.S. (2002) A continental back-arc setting for Early to Middle
908   Proterozoic basins of northeastern Australia. Geology, 30, 823–826.

909   Gordon, G.W., Lyons, T.W., Arnold, G.L., Roe, J., Sageman, B.B., and Anbar, A.D. (2009)
910   When do black shales tell molybdenum isotope tales? Geology, 37, 535–538.

911   Gorter, G., and Grey, K. (2012) Velkerri Formation: Depositional Model – Beetaloo
912   Subbasin, Northern Territory, Australia: Biostratigraphy and Organic Enrichment. Central
913   Australian Basins Symposium, Alice Springs, Australia.

914   Gregory, D., Meffre, S., and Large, R. (2014) Comparison of metal enrichment in pyrite
915   framboids from a metal-enriched and metal-poor estuary. American Mineralogist, 99 (4),
916   633-644.

917   Gregory, D.D., Large, R.R., Halpin, J.A., Lounejeva, E.B., Lyons, T.W., Wu, S., Sack, P.J.,
918   Chappaz, A., Maslennikov, V.V., Bull, S.W., and Danyushevsky, L. (2015a) Trace element
919   content of sedimentary pyrite in black shales. Economic Geology, 110, 1389–1410.

920   Gregory, D.D., Large, R.R., Halpin, J.A., Steadman, J.A., Hickman, A.H., Ireland, T.R., and
921   Holden, P. (2015b) The chemical conditions of the late Archean Hamersley basin inferred
922   from whole rock and pyrite geochemistry with Δ 33 S and δ 34 S isotope analyses.
923   Geochimica et Cosmochimica Acta, 149, 223-250.

924   Gregory, D.D., Lyons, T.W., Large, R.R., Jiang, G., Stepanov, A.S., Diamond, C., Figueroa,
925   M., and Olin, P. (2017) Whole rock and discrete pyrite geochemistry as complementary
926   tracers of ancient ocean chemistry: An example from the Neoproterozoic Doushantuo
927   Formation,   China: Geochimica   et   Cosmochimica   Acta,
928   http://dx.doi.org/10.1016/j.gca.2017.05.042
929
930   Huang, P.M., and Germida, J.J. (2002) Chemical and biochemical processes in the
931   rhizosphere: metal pollutants. In Interactions Between Soil Particles and Microorganisms:
932   Impact on the Terrestrial Ecosystem, ed. Huang, P.M., Bollag, J.M., and Senesi, N., p. 381-

933   438, Wiley, New York.

934   Huerta-Diaz, M.A., and Morse, J.W. (1992) Pyritization of trace metals in anoxic marine
935   sediments. Geochimica et Cosmochimica Acta, 56, 2681–2702

936   Ireland, T.R., Schram, N., Holden, P., Lanc, P., Ávila, J., Armstrong, R., Amelin, Y.,
937   Latimore, A., Corrigan, D., Clement, S., Foster, J.J., and Compston, W. (2014) Charge-mode
938   electrometer measurements of S-isotopic compositions on SHRIMP-SI. International Journal
939   of Mass Spectrometry, 359, 26-37.
940
941   Ireland, T., Clement, S., Compston, W., Foster, J., Holden, P., Jenkins, B., Lanc, P., Schram,
942   N., and Williams, I. (2008) Development of SHRIMP. Australian Journal of Earth Sciences,
943   55, 937–954.
944
945   Jackson, M.J. (1985) Mid-Proterozoic dolomitic varve sand microcycles from the McArthur
946   Basin, northern Australia. Sedimentary Geology, 44, 301–326.
947
948   Jackson, M.J., and Raiswell, R. (1991) Sedimentology and carbon-sulphur geochemistry of
949   the Velkerri Formation, a Mid- Proterozoic potential oil source in northern Australia.
950   Precambrian Research, 54, 81–108.

951   Jackson, M.J., and Southgate, P.N. (2000) Evolution of three unconformity-bounded sandy
952   carbonate successions in the McArthur River region of northern Australia: the Lawn, Wide
953   and Doom Supersequences in the proximal part of the Isa SuperBasin. Australian Journal of
954   Earth Sciences, 47, 600–625.

955   Jackson, T.A. (1998) The biogeochemical and ecological significance of interactions between
956   colloidal minerals and trace elements. In Environmental Interactions of Clays, ed. Parker, A.,
957   and Rae, J.E., p. 93-205, Springer-Verlag.

958   Jãrgensen, B.B., Bãttcher, M.E., Lãschen, H., Neretin, L.N., Volkov, I.I. (2004) Anaerobic
959   methane oxidation and a deep H_2S sink generate isotopically heavy sulfides in Black Sea
960   sediments 1. Geochimica et Cosmochimica Acta, 68, 2095-2118.

961   Javaux, E.J., Knoll, A.H., and Walter, M.R. (2001) Morphological and ecological complexity
962   in early eukaryotic ecosystems. Nature, 412, 66–69.

963   Javaux, E., Knoll, A.H., and Walter, M.R. (2004) TEM evidence for eukaryotic diversity in
964   mid-Proterozoic oceans. Geobiology, 2, 121–132.

965   Jochum, K.P., Pfänder, J., Woodhead, J.D., Willbold, M., Stoll, B., Herwig, K., Amini, M.,
966   Abouchami, W., and Hofmann, A.W. (2005) MPI-DING glasses: New geological reference
967   materials for in situ Pb isotope analysis. Geochemistry Geophysics Geosystems, 6, 1525-
968   2027.
969
970   Johnston, D.T., Farquhar, J., Summons, R.E., Shen, Y., Kaufman, A.J., Masterson, A.L., and
971   Canfield, D.E. (2008) Sulfur isotope biogeochemistry of the Proterozoic McArthur Basin.
972   Geochimica et Cosmochimica Acta, 72, 4278–4290.

973 Jones, B., and Manning, D.A.C. (1994) Comparison of geochemical indices used for the
974 interpretation of palaeoredox conditions in ancient mudstones. Chemical Geology, 111, 111 –
975 129.
976
977 Kah, L.C., Lyons, T.W., and Frank, T.D. (2004) Low marine sulphate and protracted
978 oxygenation of the Proterozoic biosphere. Nature, 431, 834–838.

979 Kendall, B., Creaser, R.A., Gordon, G.W., and Anbar, A.D. (2009) Re-Os and Mo isotope
980 systematics of black shales from the Middle Proterozoic Velkerri and Wollogorang
981 Formations, McArthur Basin, northern Australia. Geochimica et Cosmochimica Acta, 73,
982 2534-2558.
983
984 Khan, M.B., Masiol, M., Hofer, A., and Pavoni, B. (2014) Harmful Elements in Estuarine
985 and Coastal Systems (chapter 2) in C. Bini and J. Bech (eds.), PHEs, Environment and
986 Human Health, 37, DOI 10.1007/978-94-017-8965-3_2.
987
988 Konhauser, K.O., Pecoits, E., Lalonde, S.V., Papineau, D., Nisbet, E.G., Barley, M.E.,
989 Arndt, N.T., Zahnle, K., and Kamber, B.S. (2009) Oceanic nickel depletion and a
990 methanogen famine before the Great Oxidation Event. Nature, 458, 750–753.
991
992 Large, R.R., Gregory, D.D., Steadman, J.A., Tomkins, A.G., Lounejeva, E., Danyushevsky,
993 L. V., Halpin, J.A., Maslennikov, V.V., Sack, P.J., Mukherjee, I., and Hickman, A. (2015a)
994 Gold in the oceans through time. Earth and Planetary Science Letters, 428, 139-150.

995 Large, R.R, Halpin J.A., Lounejeva, E., Danyushevsky, L.V., Maslennikov, V.V., Gregory,
996 D., Sack, P.J., Haines, P.W., Long, J.A., Makoundi, C., and Stepanov, A.S. (2015b) Cycles of
997 nutrient trace elements in the Phanerozoic ocean, Gondwana Research, 28 (4), 1282-1293.
998
999 Large, R.R., Mukherjee, I., Gregory, D.D., Steadman, J.A., Maslennikov, V.V., and Meffre,
1000 S. (2017) Ocean and Atmosphere Geochemical Proxies Derived from Trace Elements in
1001 Marine Pyrite: Implications for Ore Genesis in Sedimentary Basins. Economic Geology,
1002 112(2), 423-450

1003 Large, R.R., Danyushevsky, L., Hollit, C., Maslennikov, V., Meffre, S., Gilbert, S., Bull, S.,
1004 Scott, R., Emsbo, P., Thomas, H., Singh, B., and Foster, J. (2009) Gold and trace element
1005 zonation in pyrite using a laser imaging technique: Implications for the timing of gold in
1006 orogenic and carlin-style sediment-hosted deposits. Economic Geology, 104, 635–668
1007
1008 Large R.R., Halpin, J.A., Danyushevsky, L.V., Maslennikov, V.V., Bull, S.W., Long, J.A.,
1009 Gregory, D.D., Lounejeva, E., Lyons, T.W., Sack, P.J., McGoldrick, P., and Calver, C.R.
1010 (2014) Trace element content of sedimentary pyrite as a new proxy for deep-time ocean-
1011 atmosphere evolution. Earth and Planetary Science Letters, 389, 209-220.

1012 Large, R.R., Maslennikov, V.V., Robert, F., Danyushevsky, L.V., and Chang, Z. (2007)
1013 Multi stage sedimentary and metamorphic origin of pyrite and gold in the Giant Sukhoi log
1014 deposit, Lena Gold Province, Russia. Economic Geology, 102, 1233–1267.
1015

1016   Leavitt, W.D., Bradley, A.S., Halevy, I., Johnston, D.T. (2013) Influence of sulfate reduction
1017   rates on the Phanerozoic sulfur isotope record. Proceedings of the National Academy of
1018   Sciences, 110, 11244–11249
1019
1020   Lee, D.S., Edmond, J.M., and Bruland, K.W. (1985/1986) Bismuth in the Atlantic and North
1021   Pacific Ocean: A natural analogue to plutonium and lead? Earth and Planetary Science
1022   Letters, 76, 254–262.
1023
1024   Lin, Z., Sun, X., Peckmann, J., Lu, Y., Xu, L., Strauss, H., Zhou, H., Gong, J., Lu, H.,
1025   Teichert, B.M.A. (2016) How sulfate-driven anaerobic oxidation of methane affects the
1026   sulfur isotopic composition of pyrite: A SIMS study from the South China Sea. Chemical
1027   Geology, 440, 26-41.
1028
1029   Lindsay, J.F., and Brasier, M.D. (2000) A carbon isotope reference curve for ca. 1700-1575
1030   Ma, McArthur and Mount Isa Basins, northern Australia. Precambrian Research, 99 (3-4),
1031   271-308.

1032   Liu, X., Fike, D., Li, A., Dong, J., Xu, F., Zhuang, G., Rendle-Buhring, R., and Wan, S.
1033   (2019) Pyrite sulfur isotopes constrained by sedimentation rates: Evidence from sediments on
1034   the East China Sea inner shelf since the late Pleistocene. Chemical Geology, 505, 66–75

1035   Logan, G.A., Hayes, J.M., Hieshima, G.B., and Summons, R.E. (1995) Terminal Proterozoic
1036   reorganization of biogeochemical cycles. Nature, 376, 53–56.

1037   Longerich, H.P., Jackson, S.E., and Günthe , D. (1996) Laser ablation inductively coupled
1038   plasma mass spectrometric transient signal data acquisition and analyte concentration
1039   calculation. Journal of Analytical Atomic Spectrometry, 11, 899-904.

1040   Luo, G., Ono, S., Huang, J., Algeo, T.J., Li, C., Zhou, L., Robinson, A., Lyons, T.W., and
1041   Xie, S. (2015) Decline in oceanic sulphate levels during the early Mesoproterozoic.
1042   Precambrian Research, 258, 36-47.

1043   Lyons, T.W., Gellatly, A.M., Goldrick, P.J., and Kah, L.C. (2006) Proterozoic sedimentary
1044   exhalative (SEDEX) deposits and links to evolving global ocean chemistry. Geological
1045   Society of America, 198, 169–184.

1046   Lyons, T.W., Reinhard, C.T., and Planavsky, N.J. (2014) The rise of oxygen in Earth's early
1047   ocean and atmosphere. Nature, 506, 307-315.

1048   Lyons, T.W., Werne, J.P., Hollander, D.J., and Murray, R.W. (2003) Contrasting S
1049   geochemistry and Fe/Al and Mo/Al ratios across the last oxic to anoxic transition in the
1050   Cariaco Basin, Venezuela. Chemical Geology, 195, 131–157.
1051
1052   McLennan, S.M., and Taylor, S.R. (1991) Sedimentary rocks and crustal evolution revisited:
1053   Tectonic setting and secular trends. Journal of Geology, 99, 1–21

1054   McLennan, S.M., Taylor, S.R., McCulloch, M.T., and Maynard, J.B. (1990) Geochemical
1055   and Nd – Sr isotopic composition of deep-sea turbidites: Crustal evolution and plate tectonic
1056   associations. Geochimica et Cosmochimica Acta, 54, 2015–2050.

1057   McKenzie, R.M. (1972) The sorption of some heavy metals by the lower oxides of
1058   manganese. Geoderma, 8, 29-35.

1059   Meyer, K.M., and Kump, L.R. (2008) Oceanic euxinia in Earth history: Causes and
1060   consequences. Annual Review of Earth and Planetary Sciences, 36, 251–88.

1061   Morford, J.L., Russell, A.D., and Emerson, S. (2001) Trace metal evidence for changes in the
1062   redox environment associated with the transition from terrigenous clay to diatomaceous
1063   sediment, Saanlich Inlet, BC. Marine Geology, 174, 355– 369.
1064

1065   Morita, M., Uemoto, H., Watanabe, A. (2007) Reduction of selenium oxyanions in
1066   wastewater using two bacterial strains. Engineering in Life Sciences, 7 (3), 235–240.
1067

1068   Morse, J.W., and Arakaki, T. (1993) Adsorption and coprecipitation of divalent metals with
1069   mackinawite (FeS). Geochimica et Cosmochimica Acta, 57, 3635–3640
1070

1071   Mukherjee, I., and Large, R. (2016) Pyrite trace element chemistry of the Velkerri Formation,
1072   Roper Group, McArthur Basin: Evidence for atmospheric oxygenation during the Boring
1073   Billion. Precambrian Research, 281, 13-26
1074

1075   Mukherjee, I., and Large, R. (2017) Application of pyrite trace element chemistry to
1076   exploration for SEDEX style Zn-Pb deposits: McArthur Basin, Northern Territory, Australia.
1077   Ore Geology Reviews, 81, 1249-1270.
1078

1079   Mukherjee, I., Large, R., Corkrey, R., and Danyushevsky, L. (2018) The Boring Billion, a
1080   slingshot to complex life on Earth. Scientific Reports, 8, Article number 4432.
1081

1082   Munson, T.J. (2016) Sedimentary characterisation and correlation of the Wilton package,
1083   greater McArthur Basin: in Annual Geoscience Exploration Seminar (AGES) presentations,
1084   Alice Springs, Northern Territory 15–16 March 2016. Northern Territory Geological Survey,
1085   Record 2016-001.
1086

1087   Murray, J.W. (1968) The adsorption of aqueous metal on colloidal hydrous manganese oxide.
1088   Advances in Chemistry, 79, 74–81.
1089

1090   Murray, J.W. (1975) The interaction of cobalt with hydrous manganese dioxide. Geochimica
1091   et Cosmochimica Acta, 39, 635–647.
1092

1093   Nishri, A., and Halicz, L. (2014). Dynamics of redox sensitive elements. Chap. 28. In:
1094   Zohary, T., Sukenik, A., Berman, T., Nishri, A. (eds.), Lake Kinneret: Ecology and
1095   Management. Springer, Heidelberg.
1096

1097   Norman, M., Pearson, N.J., Sharma, A., Griffin, W.L. (1996) Quantitative analysis of trace
1098   elements in geological materials by laser ablation ICPMS: instrumental operating conditions
1099   and calibration values of NIST glasses. Geostandards and Geoanalytical Research, 20 (2),
1100   247-261
1101

1102   Page, R.W., Jackson, M.J., and Krassay, A.A. (2000) Constraining the sequence stratigraphy
1103   in northern Australian basins: SHRIMP U-Pb zircon geochronology between Mt Isa and
1104   McArthur River. Australian Journal of Earth Sciences, 47 (3), 431–460.

1105

1106   Page, R.W., and Sweet, I.P. (1998) Geochronology of Basin phases in the western Mt Isa
1107   Inlier and correlation with the McArthur Basin. Australian Journal of Earth Sciences, 45(2),
1108   201–232.

1109   Pailler, D., Bard, E., Rostek, F., Zheng, Y., Mortlock, R., and Van Geen, A. (2002) Burial of
1110   redox-sensitive metals and organic matter in the equatorial Indian Ocean linked to precession.
1111   Geochimica et Cosmochimica Acta, 66, 849– 865.

1112

1113   Partin, C.A., Bekker, A., Planavsky, N.J., Scott, C.T., Gill, B.C., Li, C., Podkovyrov, V.,
1114   Maslov, A., Konhauser, K.O., Lalonde, S.V., Love, G.D., Poulton, S.W., and Lyons, T.W.
1115   (2013) Large-scale fluctuations in Precambrian atmospheric and oceanic oxygen levels from
1116   the record of U in shales. Earth and Planetary Science Letters, 369–370.

1117   Pasquier, V., Sansjofre, P., Rabineau, M., Revillon, S., Houghton, J., and Fike, D. (2017)
1118   Pyrite sulfur isotopes reveal glacial−interglacial environmental changes. Proceedings of the
1119   National Academy of Sciences, 114, 5941–5945

1120   Pickering, W. (1979) Copper retention by sediment/soil components. In Copper in the
1121   Environment Vol. I, Ecological Cycling, ed. Nriagu, J.O., p. 217-253, Wiley, New York.

1122   Planavsky, N.J., McGoldrick, P., Scott, C.T., Li, C., Reinhard, C.T., Kelly, A.E., Chu, X.,
1123   Bekker, A., Love, G.D., and Lyons, T.W. (2011) Widespread iron-rich conditions in the mid-
1124   Proterozoic ocean. Nature, 447, 448–451.

1125   Planavsky, N.J., Reinhard, C.T., Wang, X., Thomson, D., McGoldrick, P., Rainbird, R.H.,
1126   Johnson, T., Fischer, W.W., and Lyons, T.W. (2014) Low Mid-Proterozoic atmospheric
1127   oxygen levels and the delayed rise of animals. Science, 346, 635-638.

1128   Plumb, K.A. (1979a) Structure and tectonic style of the Precambrian shields and platforms of
1129   northern Australia. Tectonophysics, 58, 291-325.

1130

1131   Plumb, K.A. (1979b) The tectonic evolution of Australia. Earth Science Reviews, 14, 205-
1132   249.

1133

1134   Rawlings, D.J. (1999) Stratigraphic resolution of a multiphase intracratonic Basin system: the
1135   McArthur Basin, northern Australia. Australian Journal of Earth Sciences, 46, 703–723.

1136   Reimann, C., and De Caritat, P. (1998) Chemical Elements in the Environment, Fact Sheets
1137   for the Geochemist and Environmental Scientist, 397 p. Springer-Verlag, Berlin.

1138   Reinhard, C.T., Planavsky, N.J., Robbins, L.J., Partin, C.A., Gill, B.C., Lalonde, S.V.,
1139   Bekker, A., Konhauser, K.O., and Lyons, T.W. (2013) Proterozoic ocean redox and
1140   biogeochemical stasis. Proceedings of the National Academy of Sciences USA, 110, 5357–
1141   5362.

1142   Rickard, D. (2012) Sulfidic sediments and sedimentary rocks. In: Van Loon, A.J. (Ed.),
1143   Developments in Sedimentology. 801 p. Elsevier.

1144   Ries, J.B., Fike, D.A., Pratt, L.M., Lyons, T.W., and Grotzinger, J.P. (2009) Superheavy
1145   pyrite (δ34Spyr > δ34SCAS) in the terminal Proterozoic Nama Group, southern Namibia: A
1146   consequence of low seawater sulfate at the dawn of animal life. Geology, 37, 743-746.
1147
1148   Rogers, J. (1996) Geology and tectonic setting of the Tawallah Group, southern McArthur
1149   Basin, Northern Territory. PhD thesis, University of Tasmania, Australia.
1150
1151   Sahoo, S.K., Planavsky, N.J., Jiang, G., Kendall, B., Owens, J.D., Wang, X., Shi, X., Anbar,
1152   A.D., and Lyons, T.W. (2016) Oceanic oxygenation events in the anoxic Ediacaran ocean.
1153   Geobiology, 14, 457–468.

1154   Sahoo, S.K., Planavsky, N.J., Kendall, B., Wang, X., Shi, X., Scott, C., Anbar, A.D., Lyons,
1155   T.W., and Jiang, G. (2012) Ocean oxygenation in the wake of the Marinoan glaciation.
1156   Nature 489, 546–549.

1157   Smith, K.S. (1999) Metal sorption on mineral surfaces: An overview with examples relating
1158   to mineral deposits, in Plumlee, G.S., and Logsdon, M.J., eds., The environmental
1159   geochemistry of mineral deposits, Part A: Processes, techniques, and health issues, Reviews
1160   in Economic Geology, vol. 6A, Chapter 7: p. 161–182, Society of Economic Geologists, Inc.,
1161   Littleton, Colorado,

1162   Smith, K.S., and Huyck, H.L.O. (1999) An overview of the abundance, relative mobility,
1163   bioavailability, and human toxicity of metals, in Plumlee, G.S., and Logsdon, M.J., eds., The
1164   environmental geochemistry of mineral deposits, Part A: Processes, techniques, and health
1165   issues, Reviews in Economic Geology, vol. 6A, Chapter 2: Littleton, p. 29–70, Society of
1166   Economic Geologists, Inc., Colorado

1167   Scott, C., Lyons, T.W., Bekker, A., Shen, Y., Poulton, S.W., Chu, X., and Anbar, A.D.
1168   (2008) Tracing the stepwise oxygenation of the Proterozoic ocean. Nature, 452, 456–459.

1169   Shen, Y., Canfield, D.E., and Knoll, A.H. (2002) Middle Proterozoic ocean chemistry:
1170   Evidence from the McArthur Basin, northern Australia. American Journal of Science, 302,
1171   81–109.

1172   Shen, Y., Knoll, A.H., and Walter, M.R. (2003) Evidence for low sulphate and anoxia in a
1173   mid-Proterozoic marine basin. Nature, 423, 632–635.

1174   Smedley, P.L., and Kinniburgh, D.G. (2002) A review of the source, behaviour and
1175   distribution of arsenic in natural waters. Applied Geochemistry, 17, 517–568.

1176   Southgate, P.N., Bradshaw, B.E., Domagala, J., Jackson, M.J., Idnurm, M., Krassay, A.A.,
1177   Page, R.W., Sami, T.T., Scott, D.L., Lindsay, J.F., McConachie, B.A., and Tarlowski, C.
1178   (2000) Chronostratigraphic basin framework for Palaeoproterozoic rocks (1730–1575 Ma) in
1179   northern Australia and implications for base-metal mineralisation. Australian Journal of Earth
1180   Sciences, 47, 461– 483.

1181

1182   Sparks, D.L. (2003) Environmental Soil Chemistry, 2nd ed. Academic Press, San Diego, CA.
1183   pp.352

1184   Strauss, H., and Schieber, J. (1990) A sulfur isotope study of pyrite genesis: The Mid-
1185   Proterozoic Newland Formation, Belt Supergroup, Montana. Geochimica et Cosmochimica
1186   Acta, 54, 197–204.

1187   Strauss, H. (1993) The sulfur isotopic record of Precambrian sulphates: New data and a
1188   critical evaluation of the existing record. Precambrian Research, 63, 225–246.

1189   Strauss, H., and Moore, T.B. (1992) Abundances and isotopic compositions of carbon and
1190   sulfur species in whole rock and kerogen samples, in Schopf, J. W., and Kleins, C., editors,
1191   The Proterozoic Biosphere: p. 709 –798, Cambridge University Press, Cambridge.

1192   Swanner, E.D., Planavsky, N.J., Lalonde, S.V., Robbins, L.J., Bekker, A., Rouxel, O.J.,
1193   Saito, M.A., Kappler, A., Mojzsis, S.J., and Konhauser, K. (2014) Cobalt and marine redox
1194   evolution. Earth and Planetary Science Letters, 390, 253–263.

1195   Taylor, S.R., and Mclennan, S.M. (1995) The geochemical evolution of the continental crust.
1196   Reviews of Geophysics, 33, 241–265.

1197   Tribovillard, N., Algeo, T.J., Lyons, T., and Riboulleau, A. (2006) Trace metals as
1198   paleoredox and paleoproductivity proxies: an update. Chemical Geology, 232, 12–32.

1199   Violante, A., Krishnamurti, G.S.R., and Pigna, M. (2008) Mobility of Trace Elements in Soil
1200   Environments. In: A. Violante, P.M. Huang, G.M. Gadd (eds). Biophysico-Chemical
1201   Processes of Metals and Metalloids in Soil Environments, p. 169-213 John Wiley and Sons,
1202   Hoboken, New Jersey.
1203

1204   Whitehouse, M.J. (2013) Multiple S isotope determination by SIMS: Evaluation of reference
1205   sulfides for $\Delta 33S$ with observations and a case study on the determination of $\Delta 36S$.
1206   Geostandards and Geoanalytical Research, 37, 19–33.
1207

1208   Wignall, P.B. (1994) Black Shales, 127 p. Clarendon Press, Oxford.
1209

1210   Williams, R.J.P., and Rickaby R. (2012) Evolutions destiny. Co-evolution of the environment
1211   and life, 344 p. Royal Society of Chemistry, London
1212

1213   Yang, S., Kendall, B., Lu, X., Zhang, F., and Zheng, W. (2017) Uranium isotope
1214   compositions of mid-Proterozoic black shales: Evidence for an episode of increased ocean
1215   oxygenation at 1.36 Ga and evaluation of the effect of post-depositional hydrothermal fluid
1216   flow. Precambrian Research, 298. 187-201.
1217

1218   Yarincik, K.M., Murray, R.W., Lyons, T.W., Peterson, L.C., and Haug, G.H. (2000)
1219   Oxygenation history of bottom waters in the Cariaco Basin, Venezuela, over the past 578,000
1220   years: results from redox-sensitive metals (Mo, V, Mn, and Fe). Paleoceanography, 15, 593–
1221   604

1222

1223 Zerkle, A.L., House, C.H., and Brantley, S.L. (2005) Biogeochemical signatures through time

1224 as inferred from whole microbial genomes. American Journal of Science, 305, 467–502.

1225

Table 1 LA-ICP-MS pyrite analyses (geometric mean) for the Wollogorang Formation(n=46), Barney Creek Formation (n=115) and Velkerri Formation (n=55) in ppm; m=met

Formation	Depth in meters (m)	Co	Ni	Cu	Zn	As	Se	Mo	Tl	Pb	Bi	Data source
Wollogorang Formation	67.8	212	320	64	138	936	3	226	78	113	11	Mukherjee et al., 2018
Wollogorang Formation	73.8	590	511	468	103	2958	14	201	32	666	13	Mukherjee et al., 2018
Wollogorang Formation	74.3	148	314	110	75	2027	12	871	8	217	80	Mukherjee et al., 2018
Wollogorang Formation	77	354	179	744	4	8472	4	9	62	169	1.29	Mukherjee et al., 2018
Wollogorang Formation	85.4	2596	1102	964	1	6938	32	12	1	148	113	Mukherjee et al., 2018
Barney Creek Formation	47.5	183	475	109	11	965	8	357	21	970	3	Mukherjee and Large, 2017
Barney Creek Formation	54.2	76	218	59	323	262	7	59	3	236	14	Mukherjee and Large, 2017
Barney Creek Formation	60.8	94	242	102	229	393	6	79	10	222	15	Mukherjee and Large, 2017
Barney Creek Formation	68.5	53	141	92	88	375	4	106	5	114	11	Mukherjee and Large, 2017
Barney Creek Formation	70.2	775	1258	770	17	1587	24	71	23	1474	4	Mukherjee and Large, 2017
Barney Creek Formation	76.1	22	73	44	2	269	6	8	10	323	0.425	Mukherjee and Large, 2017
Barney Creek Formation	81.9	148	354	102	96	346	6	215	7	380	6	Mukherjee and Large, 2017
Barney Creek Formation	86.8	158	335	92	11	1192	8	169	15	462	9	Mukherjee and Large, 2017
Barney Creek Formation	93	160	479	293	45	1769	13	446	9	838	11	Mukherjee and Large, 2017
Barney Creek Formation	98.3	118	202	136	29	972	5	202	16	428	5	Mukherjee and Large, 2017
Barney Creek Formation	100.7	112	275	108	74	380	6	274	18	493	8	Mukherjee and Large, 2017
Barney Creek Formation	109.8	133	271	44	159	307	5	194	12	288	19	Mukherjee and Large, 2017
Barney Creek Formation	124.5	108	231	43	21	1473	5	67	51	274	18	Mukherjee and Large, 2017
Barney Creek Formation	128.4	106	170	121	9	1321	49	5	1	190	2	Mukherjee and Large, 2017
Barney Creek Formation	148.8	572	1246	240	5	7442	11	3	53	933	4	Mukherjee and Large, 2017
Velkerri Formation	115.7	2	85	48	22	20	5	5	0.412	5	1	Mukherjee and Large, 2016
Velkerri Formation	126.3	40	223	41	47	36	10	38	1	80	3	Mukherjee and Large, 2016
Velkerri Formation	140.1	40	685	100	107	7512	87	37	7	404	1	Mukherjee and Large, 2016
Velkerri Formation	151.2	34	444	64	1560	821	34	30	10	121	3	Mukherjee and Large, 2016
Velkerri Formation	161.8	187	1671	176	397	605	38	415	18	371	8	Mukherjee and Large, 2016
Velkerri Formation	172.4	22	144	39	118	1921	7	3	10	111	1	Mukherjee and Large, 2016
Velkerri Formation	183.4	105	504	104	8	4787	48	1	13	384	2	Mukherjee and Large, 2016
Velkerri Formation	193.9	85	260	112	165	173	8	14	4	97	2	Mukherjee and Large, 2016
Velkerri Formation	216.9	122	236	54	81	380	9	9	3	56	2	Mukherjee and Large, 2016

Table 2 Multiplicative standard deviation for the Wollogorang Formation (n=46), Barney Creek Formation (n=115) and Velkerri Formation (n=55) in ppm

Formation	Depth in meters (m)	Co	Ni	Cu	Zn	As	Se	Mo	Tl	Pb	Bi
Wollogorang Formation	67.8	1.27	1.09	1.11	1.84	1.07	1.15	1.06	1.19	1.28	1.04
Wollogorang Formation	73.8	1.09	1.12	1.32	1.33	1.06	1.11	1.14	1.31	1.10	1.08
Wollogorang Formation	74.3	1.07	1.08	1.21	1.04	1.28	1.18	1.24	3.11	1.52	2.12
Wollogorang Formation	77	1.37	1.34	1.49	2.46	1.37	1.39	2.12	1.19	1.37	1.51
Wollogorang Formation	85.4	1.09	1.28	1.30	3.08	1.19	1.12	1.13	1.88	1.19	1.20
Barney Creek Formation	47.5	1.65	1.57	1.26	2.68	1.49	1.18	1.18	1.38	1.68	2.74
Barney Creek Formation	54.2	1.16	1.14	1.31	1.14	1.13	1.49	1.22	1.80	1.20	1.11
Barney Creek Formation	60.8	1.11	1.11	1.31	1.29	1.14	1.33	1.32	1.48	1.10	1.15
Barney Creek Formation	68.5	1.22	1.11	1.12	1.56	1.21	1.38	1.21	1.36	1.65	2.32
Barney Creek Formation	70.2	2.46	2.04	1.55	3.07	1.33	1.41	2.15	1.60	1.39	2.42
Barney Creek Formation	76.1	1.23	1.17	1.03	1.25	1.15	1.03	1.17	1.07	1.02	1.14
Barney Creek Formation	81.9	1.08	1.10	1.06	1.42	1.14	1.15	1.10	1.10	1.06	1.05
Barney Creek Formation	86.8	1.02	1.02	1.12	1.52	1.07	1.04	1.19	1.06	1.04	1.15
Barney Creek Formation	93	1.19	1.28	1.49	1.59	1.53	1.39	1.17	1.13	1.17	1.07
Barney Creek Formation	98.3	1.01	1.02	1.05	1.11	1.04	1.07	1.05	1.04	1.03	1.05
Barney Creek Formation	100.7	1.11	1.14	1.15	1.18	1.17	1.13	1.18	1.19	1.07	1.20
Barney Creek Formation	109.8	1.11	1.05	1.08	1.37	1.08	1.76	1.31	2.14	1.08	1.09
Barney Creek Formation	124.5	1.09	1.08	1.23	1.25	1.16	1.31	1.16	1.09	1.11	1.03
Barney Creek Formation	128.4	1.26	1.35	1.52	2.35	1.56	1.29	3.09	1.97	1.25	1.51
Barney Creek Formation	148.8	1.19	1.19	1.25	1.08	1.46	1.48	2.34	1.38	1.24	1.31
Velkerri Formation	115.7	1.43	1.54	2.36	1.51	1.93	1.66	1.63	2.10	1.55	1.00
Velkerri Formation	126.3	1.56	1.42	1.36	1.14	1.33	1.51	1.24	1.27	1.23	1.25
Velkerri Formation	140.1	1.16	1.16	1.24	1.39	1.10	1.11	1.24	1.10	1.10	1.00
Velkerri Formation	151.2	2.09	1.83	1.15	1.41	1.26	1.19	1.08	1.94	1.83	1.55
Velkerri Formation	161.8	1.31	1.47	1.52	1.93	1.30	1.24	1.66	1.27	1.32	1.31
Velkerri Formation	172.4	1.67	1.72	1.41	2.60	2.86	2.06	2.50	1.25	1.67	1.14
Velkerri Formation	183.4	1.30	1.43	1.67	2.31	2.12	1.42	2.21	1.27	1.54	1.31
Velkerri Formation	193.9	1.68	1.68	2.40	1.53	2.19	1.64	2.46	2.13	1.63	1.41
Velkerri Formation	216.9	1.79	1.75	2.21	2.45	2.20	1.84	1.94	2.36	1.81	1.51

Table 3 LA-ICP-MS pyrite analyses (geometric mean) for all three black shale formations in ppm.

Formation	Age	Co	Ni	Cu	Zn	As	Se	Mo	Tl	Pb	Bi	Se/Co	Ni/Co	Zn/Co	Mo/Co	Se/Bi	Ni/Bi	Zn/Bi	Mo/Bi
Upper Velkerri (n=55)	~1360 Ma	48	387	81	96	502	19	20	5	137	2	0.40	8.00	1.98	0.42	8.29	166	41	9
Barney Creek (n=115)	~1640 Ma	138	318	120	33	772	8	79	11	419	6	0.06	2.30	0.24	0.58	1.36	51	5	13
Wollogorang (n=46)	~1730 Ma	457	377	377	28	3527	9	77	20	254	13	0.02	0.83	0.06	0.17	0.71	30.03	2.24	6.14

Table 4 Staistical t-test for equality of means in the three black shale formations; VF: Velkerri Formation, BCF: Barney Creek Formation, WF: Wollogorang Formation (See supplem

Elements	Formations	t-value	t-critical	p-value	Hypotheses of equal means ($\mu_1=\mu_2$)	Reason*	Difference in means
	VF-BCF	-3.88	1.98	0.00	Reject	-(t-critical) > t-value	significant
Mo	VF-WF	-3.19	1.98	0.00	Reject	-(t-critical) > t-value	significant
	BCF-WF	0.09	1.98	0.74	Cannot reject	t-value < (t-critical)	insignificant
	VF-BCF	4.19	1.98	0.00	Reject	t-value > (t-critical)	significant
Se	VF-WF	3.46	1.98	0.00	Reject	t-value > (t-critical)	significant
	BCF-WF	-0.33	1.98	0.58	Cannot reject	-(t-critical) < t-value	insignificant
	VF-BCF	0.99	1.98	0.32	Cannot reject	t-value < (t-critical)	insignificant
Ni	VF-WF	0.12	1.98	0.90	Cannot reject	t-value < (t-critical)	insignificant
	BCF-WF	-1.27	1.98	0.20	Cannot reject	-(t-critical) < t-value	insignificant
	VF-BCF	3.46	1.98	0.00	Reject	t-value > (t-critical)	significant
Zn	VF-WF	2.92	1.98	0.00	Reject	t-value > (t-critical)	significant
	BCF-WF	0.44	1.98	0.65	Cannot reject	t-value < (t-critical)	insignificant
	VF-BCF	-4.38	1.98	0.00	Reject	-(t-critical) > t-value	significant
Co	VF-WF	-8.82	1.98	0.00	Reject	-(t-critical) > t-value	significant
	BCF-WF	-7.31	1.98	0.00	Reject	-(t-critical) > t-value	significant
	VF-BCF	-5.66	1.98	0.00	Reject	-(t-critical) > t-value	significant
Bi	VF-WF	-5.56	1.98	0.00	Reject	-(t-critical) > t-value	significant
	BCF-WF	-2.33	1.98	0.02	Reject	-(t-critical) > t-value	significant

*Reject the hypotheses of equal means if -(t-critical) > t-value > t-critical and p < 0.10 (α)

Table 5 Black shale matrix analyses of Ti, Zr, Cr, Th in ppm and their ratios

Formation	Depth in meters	Ti	Cr	Zr	Th	Ti/Zr	Th/Cr	Data source
Velkerri Formation	115.7	254.43	1.00	67.87	5.66	3.75	5.66	This study
Velkerri Formation	126.3	1156.76	55.71	74.27	7.72	15.57	0.14	This study
Velkerri Formation	140.1	8746.43	95.92	186.07	36.59	47.01	0.38	This study
Velkerri Formation	151.2	1609.06	88.71	109.70	3.01	14.67	0.03	This study
Velkerri Formation	151.2	1407.51	92.83	44.21	1.52	31.83	0.02	This study
Velkerri Formation	151.2	111.99	17.36	7.18	5.20	15.60	0.30	This study
Velkerri Formation	151.2	1042.86	66.30	53.70	3.25	19.42	0.05	This study
Velkerri Formation	161.8	2705.62	45.95	202.31	12.76	13.37	0.28	This study
Velkerri Formation	172.4	713.61	1879.43	72.14	15.72	9.89	0.01	This study
Velkerri Formation	183.4	890.25	1.00	43.49	3.59	20.47	3.59	This study
Velkerri Formation	193.9	4580.01	419.61	194.32	8.65	23.57	0.02	This study
Velkerri Formation	216.9	3947.04	91.32	73.88	7.96	53.43	0.09	This study
					Mean	**22.38**	**0.88**	
Barney Creek Formation	47.50	4587.66	5.60	206.66	61.56	22.20	10.99	This study
Barney Creek Formation	54.20	2149.17	57.77	229.04	16.80	9.38	0.29	This study
Barney Creek Formation	60.80	4409.26	42.65	93.34	10.84	47.24	0.25	This study
Barney Creek Formation	68.50	1038.77	20.66	38.61	6.96	26.90	0.34	This study
Barney Creek Formation	70.20	77793.00	81.04	424.32	24.97	183.33	0.31	This study
Barney Creek Formation	76.10	19067.05	129.94	649.72	72.99	29.35	0.56	This study
Barney Creek Formation	81.90	3001.76	64.46	139.79	14.89	21.47	0.23	This study
Barney Creek Formation	86.80	4728.15	62.08	107.23	26.64	44.09	0.43	This study
Barney Creek Formation	93.00	3864.95	87.86	150.62	18.39	25.66	0.21	This study
Barney Creek Formation	98.30	4351.58	58.97	269.40	29.19	16.15	0.50	This study
Barney Creek Formation	100.70	3430.80	70.19	133.39	19.57	25.72	0.28	This study
Barney Creek Formation	109.80	2294.94	44.83	100.62	20.59	22.81	0.46	This study
Barney Creek Formation	124.50	1106.57	24.27	30.34	4.97	36.47	0.20	This study
Barney Creek Formation	128.40	1751.79	80.22	160.18	26.67	10.94	0.33	This study
Barney Creek Formation	136.50	20401.09	90.28	293.52	32.43	69.50	0.36	This study
Barney Creek Formation	148.80	4484.17	213.02	698.77	196.19	6.42	0.92	This study
					Mean	**37.35**	**1.04**	
Wollogorang Formation	67.8	7108.46	71.76	340.36	28.81	20.88	0.40	This study
Wollogorang Formation	73.8	818.41	42.32	49.26	7.32	16.61	0.17	This study
Wollogorang Formation	74.3	527.13	30.96	61.57	3.01	8.56	0.10	This study
Wollogorang Formation	77	468.06	1.00	7.85	1.15	59.64	1.15	This study
Wollogorang Formation	85.4	660.50	27.28	38.30	6.41	17.25	0.23	This study
					Mean	**24.59**	**0.41**	

Table 6a SHRIMPI-SI pyrite analyses for all three black shale formations in ‰ (Data source: this study)

SPOT #	$\delta^{33}S_{VCDT}$	± Internal error (2σ)	$\delta^{34}S_{VCDT}$	± Internal error (2σ)	$\Delta^{33}S$	± Internal error (2σ)	^{32}S cps (median)	^{33}S cps (median)	^{34}S cps (median)	Sets, scans
Velkerri Formation										
172.4-08-2.1	16.03	0.09	31.74	0.03	-0.20	0.10	9.5E+08	7.5E+06	4.3E+07	2, 10
172.4-08-1.1	8.60	0.07	17.45	0.04	-0.35	0.08	5.5E+08	4.4E+06	2.5E+07	2, 10
172.4-08-3.1	18.01	0.08	35.55	0.03	-0.14	0.08	1.1E+09	8.8E+06	5.0E+07	2, 10
161.8-03-1	7.92	0.15	15.74	0.04	-0.15	0.15	8.7E+08	6.8E+06	3.8E+07	2, 10
161.8-03-2	9.10	0.09	17.77	0.03	-0.01	0.09	1.0E+09	8.0E+06	4.5E+07	2, 10
161.8-03-5	7.95	0.13	16.21	0.03	-0.36	0.13	9.0E+08	7.1E+06	4.0E+07	2, 10
161.8-03-6	8.35	0.10	16.31	0.03	-0.01	0.11	9.1E+08	7.2E+06	4.0E+07	2, 10
144.3-01	12.49	0.10	24.43	0.03	-0.02	0.11	9.5E+08	7.5E+06	4.2E+07	2, 10
144.3-02	15.07	0.08	29.46	0.03	0.01	0.09	9.5E+08	7.6E+06	4.3E+07	2, 10
115.2_1	23.41	0.24	45.58	0.04	0.19	0.26	5.4E+08	4.3E+06	2.5E+07	1, 10
115.2_2	24.07	0.30	45.77	0.04	0.76	0.33	5.5E+08	4.4E+06	2.5E+07	1, 10
115.2_3	23.46	0.25	45.78	0.04	0.14	0.29	5.5E+08	4.4E+06	2.5E+07	1, 10
115.2_4	15.40	0.32	30.34	0.05	-0.11	0.33	5.6E+08	4.5E+06	2.5E+07	1, 10
115.2_5	22.25	0.16	43.95	0.04	-0.15	0.17	5.6E+08	4.5E+06	2.6E+07	1, 10
115.2_6	23.29	0.33	46.05	0.03	-0.16	0.34	5.4E+08	4.4E+06	2.5E+07	1, 10
140.1_1	11.70	0.21	22.40	0.04	0.22	0.22	5.9E+08	4.7E+06	2.6E+07	1, 10
140.1_2	11.35	0.20	22.07	0.04	0.04	0.21	5.8E+08	4.6E+06	2.6E+07	1, 10
140.1_3	11.07	0.41	22.16	0.04	-0.28	0.41	5.9E+08	4.7E+06	2.6E+07	1, 10
140.1_4	11.04	0.15	21.98	0.04	-0.22	0.16	5.9E+08	4.7E+06	2.6E+07	1, 10
140.1_5	11.46	0.22	22.50	0.04	-0.07	0.23	5.5E+08	4.4E+06	2.5E+07	1, 10
140.1_6	11.78	0.29	23.00	0.04	0.00	0.32	5.9E+08	4.7E+06	2.6E+07	1, 10
193.9-01	12.95	0.14	24.90	0.03	0.21	0.14	9.1E+08	7.3E+06	4.1E+07	2, 10
193.9-02	10.01	0.11	19.15	0.03	0.19	0.11	9.7E+08	7.7E+06	4.3E+07	2, 10
183.4-01	21.73	0.06	42.30	0.03	0.17	0.06	1.1E+09	8.7E+06	5.0E+07	2, 10
183.4-02	19.49	0.13	37.72	0.03	0.24	0.14	1.1E+09	8.8E+06	5.0E+07	2, 10
183.4-03	19.78	0.08	38.50	0.03	0.14	0.08	1.0E+09	8.0E+06	4.5E+07	2, 10
183.4-04	20.03	0.10	39.18	0.03	0.05	0.10	1.1E+09	8.7E+06	5.0E+07	2, 10
183.4-05	23.00	0.16	44.94	0.03	0.11	0.17	9.9E+08	7.9E+06	4.5E+07	2, 10
183.4-06	19.55	0.09	37.93	0.03	0.19	0.10	1.0E+09	8.2E+06	4.7E+07	2, 10
183.4-07	18.19	0.19	35.37	0.03	0.13	0.20	7.0E+08	5.6E+06	3.2E+07	2, 10
126.3-01	-3.06	0.14	-5.92	0.03	0.00	0.14	1.0E+09	8.1E+06	4.5E+07	2, 10
126.3-02	12.08	0.07	23.46	0.03	0.07	0.07	1.2E+09	9.2E+06	5.2E+07	2, 10
126.3-03	12.79	0.11	25.08	0.02	-0.05	0.12	1.2E+09	9.2E+06	5.2E+07	2, 10
126.3-04	2.62	0.10	4.95	0.02	0.07	0.10	9.7E+08	7.7E+06	4.3E+07	2, 10
126.3-05	-4.33	0.12	-8.23	0.03	-0.08	0.13	9.7E+08	7.6E+06	4.2E+07	2, 10
126.3-06	12.50	0.11	24.35	0.03	0.03	0.11	9.2E+08	7.3E+06	4.1E+07	2, 10
126.3-07	-3.26	0.14	-6.64	0.03	0.17	0.16	9.8E+08	7.7E+06	4.3E+07	2, 10
126.3-07	7.87	0.08	15.26	0.03	0.04	0.09	9.7E+08	7.6E+06	4.3E+07	2, 10
374.4-01	22.50	0.08	43.92	0.02	0.11	0.09	9.3E+08	7.4E+06	4.2E+07	2, 10
374.4-2	24.35	0.11	47.75	0.03	0.04	0.12	9.7E+08	7.8E+06	4.4E+07	2, 10
374.4-3	33.29	0.12	65.59	0.02	0.03	0.13	9.9E+08	8.1E+06	4.6E+07	2, 10
374.4-4	24.91	0.10	48.56	0.03	0.19	0.11	1.1E+09	8.6E+06	4.9E+07	2, 10
374.4-5	22.75	0.13	44.26	0.03	0.19	0.15	9.9E+08	8.0E+06	4.5E+07	2, 10
374.4-6	22.72	0.12	44.10	0.03	0.24	0.13	1.0E+09	8.2E+06	4.7E+07	2, 10
374.4-7	24.48	0.12	48.02	0.03	0.03	0.13	9.8E+08	7.9E+06	4.5E+07	2, 10
374.4-8	24.79	0.06	48.37	0.03	0.16	0.06	1.0E+09	8.3E+06	4.7E+07	2, 10
374.4-9	-7.36	0.07	-14.19	0.03	-0.02	0.07	1.1E+09	8.5E+06	4.7E+07	2, 10
374.4-10	26.93	0.09	52.79	0.03	0.08	0.10	1.0E+09	8.1E+06	4.6E+07	2, 10
183.4-01	12.28	0.09	24.14	0.03	-0.08	0.09	1.1E+09	8.4E+06	4.8E+07	2, 10
183.4-02	11.35	0.10	22.32	0.02	-0.08	0.11	1.4E+09	1.1E+07	6.4E+07	2, 10
151.2-01	11.83	0.24	22.89	0.03	0.11	0.25	5.7E+08	4.5E+06	2.5E+07	2, 10
151.2-02	13.54	0.08	26.68	0.03	-0.12	0.07	1.0E+09	8.0E+06	4.5E+07	2, 10
151.2-03	11.11	0.11	21.72	0.03	-0.01	0.12	7.2E+08	5.7E+06	3.2E+07	2, 10
151.2-04	12.15	0.10	23.80	0.03	-0.04	0.10	7.7E+08	6.1E+06	3.5E+07	2, 10
151.2-05	13.55	0.19	26.35	0.03	0.06	0.19	7.1E+08	5.7E+06	3.2E+07	2, 10
328.1-01	2.05	0.09	4.03	0.03	-0.03	0.09	9.3E+08	7.3E+06	4.1E+07	2, 10
328.1-02	3.57	0.13	7.29	0.02	-0.18	0.13	1.1E+09	8.7E+06	4.9E+07	2, 10
328.1-03	3.18	0.07	6.54	0.04	-0.19	0.07	8.1E+08	6.4E+06	3.6E+07	2, 10
328.1-04	2.02	0.11	4.03	0.04	-0.05	0.11	7.7E+08	6.0E+06	3.4E+07	2, 10
316.8_3	7.23	0.16	14.81	0.03	-0.37	0.16	6.3E+08	4.9E+06	2.8E+07	1, 10
316.8_1	7.58	0.15	14.98	0.04	-0.10	0.17	6.4E+08	5.1E+06	2.8E+07	1, 10
316.8_2	14.52	0.15	28.65	0.04	-0.14	0.15	5.0E+08	4.0E+06	2.3E+07	1, 10
			Mean	26.87		**0.01**				
			Std. Dev	16.48		**0.18**				
			Std. Error	2.09		0.02				
			Max	65.59		0.76				
			Min	-14.19		-0.37				

Table 6c SHRIMPI-SI pyrite analyses for all three black shale formations in ‰ (Data source: this study)

SPOT #	$\delta^{33}S_{VCDT}$	± Internal error (2σ)	$\delta^{34}S_{VCDT}$	± Internal error (2σ)	$\Delta^{33}S$	± Internal error (2σ)	^{32}S cps (median)	^{33}S cps (median)	^{34}S cps (median)	Sets, scans
Wollogorang Formation										
MTY_67.8_1	3.84	0.10	2.47	0.04	2.57	0.09	5.8E+08	4.6E+06	2.6E+07	1, 10
MTY_70.4_1	2.10	0.10	4.19	0.04	-0.05	0.10	5.7E+08	4.5E+06	2.5E+07	1, 10
MTY_70.4_B2	-1.62	0.24	-3.32	0.04	0.09	0.25	5.4E+08	4.2E+06	2.3E+07	1, 10
MTY_70.4_B3	-1.38	0.24	-2.21	0.03	-0.24	0.26	5.7E+08	4.4E+06	2.5E+07	1, 10
MTY_70.4_B4	-0.16	0.27	-1.10	0.04	0.41	0.28	5.4E+08	4.2E+06	2.4E+07	1, 10
MTY_70.4_B5	-0.61	0.14	-1.04	0.04	-0.08	0.15	5.7E+08	4.4E+06	2.5E+07	1, 10
MTY_70.4_B6	-2.47	0.25	-4.63	0.04	-0.08	0.29	5.6E+08	4.4E+06	2.4E+07	1, 10
MTY_77_1	-13.79	0.18	-27.92	0.04	0.69	0.18	5.3E+08	4.1E+06	2.3E+07	1, 10
MTY_77_10	-12.65	0.10	-25.57	0.05	0.60	0.10	4.3E+08	3.3E+06	1.8E+07	1, 10
MTY_77_11	1.45	0.10	1.24	0.04	0.81	0.11	4.7E+08	3.7E+06	2.1E+07	1, 10
MTY_77_12	-13.98	0.26	-28.24	0.04	0.67	0.28	5.8E+08	4.5E+06	2.5E+07	1, 10
MTY_77_2	-12.70	0.15	-25.59	0.04	0.56	0.15	5.8E+08	4.5E+06	2.5E+07	1, 10
MTY_77_3	-8.27	0.22	-16.63	0.04	0.33	0.23	5.5E+08	4.3E+06	2.4E+07	1, 10
MTY_77_4	2.99	0.10	5.26	0.04	0.28	0.10	5.5E+08	4.3E+06	2.4E+07	1, 10
MTY_77_5	2.16	0.15	3.85	0.04	0.18	0.16	5.1E+08	4.0E+06	2.2E+07	1, 10
MTY_77_6	-13.74	0.13	-27.07	0.04	0.29	0.14	5.1E+08	3.9E+06	2.2E+07	1, 10
MTY_77_7	-9.30	0.16	-19.25	0.04	0.67	0.17	5.2E+08	4.0E+06	2.2E+07	1, 10
MTY_77_8	-14.70	0.22	-29.44	0.05	0.57	0.23	4.8E+08	3.7E+06	2.1E+07	1, 10
MTY_77_9	-13.15	0.22	-26.78	0.04	0.74	0.24	4.7E+08	3.6E+06	2.0E+07	1, 10
MTY_89_B1	1.89	0.30	3.50	0.03	0.09	0.31	8.4E+08	6.6E+06	3.7E+07	1, 10
MTY_89_B2	3.44	0.19	5.66	0.03	0.53	0.19	8.9E+08	7.0E+06	3.9E+07	1, 10
MTY_89_B3	2.57	0.34	4.45	0.02	0.27	0.37	1.0E+09	8.1E+06	4.5E+07	1, 10
MTY_89_B4	3.22	0.29	5.25	0.03	0.52	0.33	9.7E+08	7.6E+06	4.2E+07	1, 10
MTY_89_B5	2.89	0.24	5.25	0.02	0.19	0.29	1.0E+09	7.9E+06	4.4E+07	1, 10
MTY_89_B6	1.23	0.12	2.69	0.03	-0.16	0.11	8.3E+08	6.5E+06	3.6E+07	1, 10
MT_YOUNG_4	4.82	0.35	9.49	0.03	-0.02	0.32	8.9E+08	7.0E+06	4.0E+07	1, 10
MT_YOUNG_1	3.73	0.29	6.65	0.02	0.34	0.23	9.3E+08	7.3E+06	4.1E+07	1, 10
MT_YOUNG_5	3.16	0.28	5.63	0.03	0.30	0.24	9.2E+08	7.2E+06	4.1E+07	1, 10
MT_YOUNG_6	3.62	0.16	7.10	0.02	0.01	0.09	9.4E+08	7.4E+06	4.1E+07	1, 10
MT_YOUNG_3	2.37	0.33	5.25	0.03	-0.30	0.27	8.9E+08	7.0E+06	3.9E+07	1, 10
MT_YOUNG_2	2.79	0.21	4.90	0.04	0.30	0.13	9.2E+08	7.2E+06	4.1E+07	1, 10
		Mean	-5.03		0.36					
		Std. Dev	13.62		0.51					
		Std. Error	2.45		0.09					
		Max	9.49		2.57					
		Min	-29.44		-0.30					

Table 6b SHRIMPI-SI pyrite analyses for all three black shale formations in ‰ (Data source: this study)

SPOT #	$\delta^{33}S_{VCDT}$	± Internal error (2σ)	$\delta^{34}S_{VCDT}$	± Internal error (2σ)	$\Delta^{33}S$	± Internal error (2σ)	^{32}S cps (median)	^{33}S cps (median)	^{34}S cps (median)	Sets, scans
Barney Creek Formation										
MBX_47.50_B1	-2.13	0.15	-4.76	0.05	0.33	0.15	6.2E+08	4.8E+06	2.7E+07	1, 10
MBX_47.50_B2	-3.30	0.17	-6.83	0.04	0.23	0.18	7.0E+08	5.5E+06	3.0E+07	1, 10
MBX_47.50_B3	-2.82	0.31	-5.28	0.04	-0.09	0.33	6.1E+08	4.8E+06	2.7E+07	1, 10
MBX_47.50_B4	4.39	0.32	8.83	0.04	-0.15	0.34	5.8E+08	4.5E+06	2.5E+07	1, 10
MBX_47.50_B5	7.41	0.11	14.71	0.04	-0.14	0.11	5.7E+08	4.5E+06	2.5E+07	1, 10
MBX_47.50_B6	-7.17	0.32	-13.79	0.05	-0.05	0.34	5.7E+08	4.5E+06	2.5E+07	1, 10
MBX124.5_1	17.92	0.25	34.68	0.04	0.21	0.25	4.6E+08	3.6E+06	2.1E+07	1, 10
MBX22.7_2	4.18	0.55	7.79	0.12	0.17	0.55	1.1E+08	8.7E+05	4.9E+06	1, 10
MBX22.7_4	5.93	0.19	12.01	0.04	-0.23	0.20	4.6E+08	3.6E+06	2.0E+07	1, 10
MBX30.10_7B	13.76	0.18	26.50	0.03	0.20	0.20	6.0E+08	4.8E+06	2.7E+07	1, 10
MBX30.10_1B	8.97	0.17	17.11	0.03	0.19	0.19	6.2E+08	4.9E+06	2.7E+07	1, 10
MBX30.10_2B	9.76	0.31	18.30	0.03	0.38	0.34	6.2E+08	4.9E+06	2.8E+07	1, 10
MBX30.10_3B	10.06	0.17	19.84	0.03	-0.11	0.18	6.5E+08	5.2E+06	2.9E+07	1, 10
MBX30.10_4B	-0.10	0.12	0.17	0.04	-0.19	0.14	6.2E+08	4.9E+06	2.7E+07	1, 10
MBX30.10_5B	-6.72	0.45	-12.88	0.04	-0.06	0.49	6.4E+08	5.0E+06	2.8E+07	1, 10
MBX30.10_6B	-4.80	0.29	-9.35	0.03	0.03	0.31	6.3E+08	4.9E+06	2.7E+07	1, 10
MBX-76.10_1	17.73	0.15	33.55	0.06	0.59	0.17	3.8E+08	3.0E+06	1.7E+07	1, 6
MBX-76.10_2	17.87	0.31	34.59	0.08	0.20	0.36	3.5E+08	2.8E+06	1.6E+07	1, 6
MBX-76.10_3	19.17	0.44	36.35	0.07	0.61	0.53	3.6E+08	2.9E+06	1.6E+07	1, 6
MBX-76.10_4	18.47	0.21	35.76	0.07	0.21	0.20	3.7E+08	2.9E+06	1.7E+07	1, 6
MBX-76.10_5	18.08	0.05	35.45	0.07	-0.02	0.06	3.6E+08	2.9E+06	1.6E+07	1, 6
MBX-76.10_6	16.69	0.12	32.33	0.06	0.17	0.12	3.7E+08	2.9E+06	1.7E+07	1, 6
MBX-76.10_7	17.33	0.41	33.69	0.08	0.11	0.47	3.6E+08	2.9E+06	1.6E+07	1, 6
MBX-76.10_8	16.47	0.06	32.12	0.08	0.06	0.06	3.7E+08	2.9E+06	1.7E+07	1, 6
MBX-76.10_9	17.39	0.14	33.06	0.08	0.50	0.14	3.6E+08	2.9E+06	1.6E+07	1, 6
MBX98.30_1	19.43	0.36	37.21	0.08	0.44	0.41	2.5E+08	2.0E+06	1.1E+07	1, 6
MBX98.30_2	11.69	0.37	22.50	0.10	0.17	0.38	2.7E+08	2.1E+06	1.2E+07	1, 6
MBX98.30_2B	10.52	0.21	21.85	0.07	-0.67	0.24	2.7E+08	2.1E+06	1.2E+07	1, 6
MBX98.30_4	20.24	0.29	39.89	0.06	-0.10	0.36	2.9E+08	2.3E+06	1.3E+07	1, 6
MBX98.30_5	19.94	0.35	39.23	0.10	-0.07	0.43	2.0E+08	1.6E+06	9.1E+06	1, 6
MBX98.30_6	20.99	0.98	41.80	0.13	-0.32	1.15	1.6E+08	1.2E+06	7.1E+06	1, 6
		Mean	**19.88**		**0.08**					
		Std. Dev	**17.74**		**0.28**					
		Std. Error	3.19		0.05					
		Max	41.80		0.61					
		Min	-13.79		-0.67					

Table 7 General characteristics of some chemical elements in simple surface or near-surface aqueous systems (modified after Smith and Huyck, 1999); n

ELEMENT	IONIC FORM	Species		REDOX-SENSITIVE; References	Type
		Oxic	Reduced		
Arsenic (As)	anionic	$H_2AsO_4^-$ or $HAsO_4^{2-}$	$H_3AsO_3^0$	(Smith and Huyck, 1999; Hinkle and Polette, 1999; Hem et al., 1985)	n
Molybdenum (Mo)	anionic; cationic species exist but are rare in aqueous systems.	MoO_4^{2-}, MoO_2^+;	$MoO_xS_{4-x}^2$ MoS_4^{2-}	(Smith and Huyck, 1999; Algeo and Maynard, 2006)	c, n
Selenium (Se)	anionic	SeO_4^{2-}, SeO_3^{2-}	Se^0	(Smith and Huyck, 1999; Morita et al., 2007)	n
Nickel (Ni)	cationic	Ni^{2+}, $Ni^{1-, 1+, 3+, 4+}$, $NiCl^+$	NiS	(Khan et al., 2014; Young 1995; Clayton and Clayton 1994; Coogan et al. 1989; Barciela-Alonso et al., 2003)	n
Zinc (Zn)	cationic	Zn^{2+}, $ZnCl^+$	ZnS	(Algeo and Maynard, 2006)	n
Bismuth (Bi)	cationic	Bi^{3+}, BiO^+ BiO^{2+}, $BiOH^2$	Bi_2S_3	(Brookins., 1988)	s
Cobalt (Co)	cationic	Co^+	CoS	(Algeo and Maynard, 2006)	s
Copper (Cu)	cationic	$CuCl^+$, Cu^{2+}, Cu^{1+}	Cu_2S, CuS	(Algeo and Maynard, 2006; Smith and Huyck, 1999)	n, s
Lead (Pb)	cationic	Pb^+, Pb^{2+}, $PbCl^+$	PbS	(redox sensitive only under extreme conditions; Smith and Huyck, 1999)	s
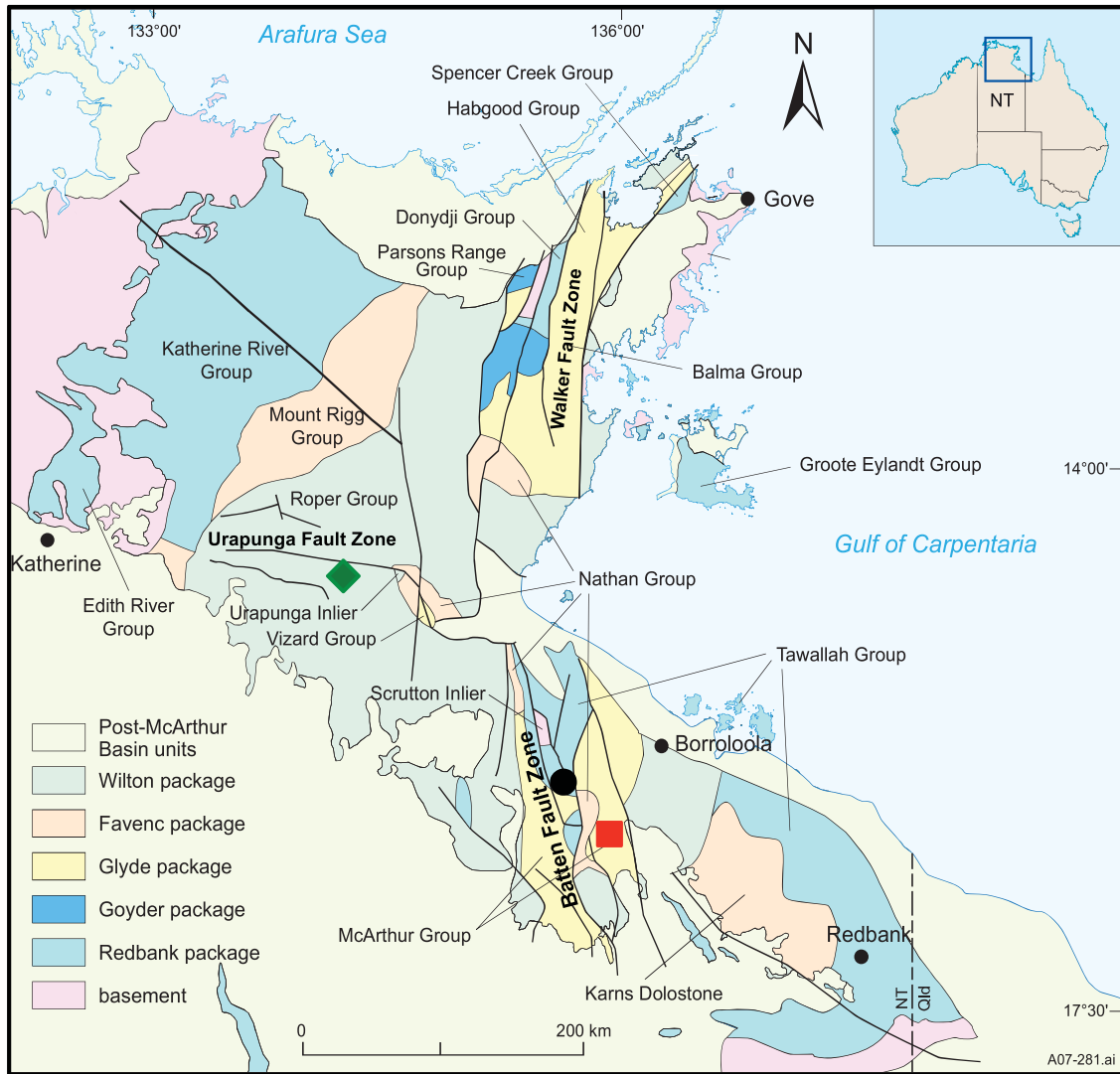
Group	Formation	Age (Ga)	Drill hole	Symbol
Roper	Velkerri	~1.4	Urap-4	🟢
McArthur	Barney Creek	~1.64	MBXDD001	🟥
Tawallah	Wollogorang	~1.73	Mt Young	⚫

Fig 1 Drill hole locations for the three black shale formations (Figure adapted from Ahmad et al., 2013)
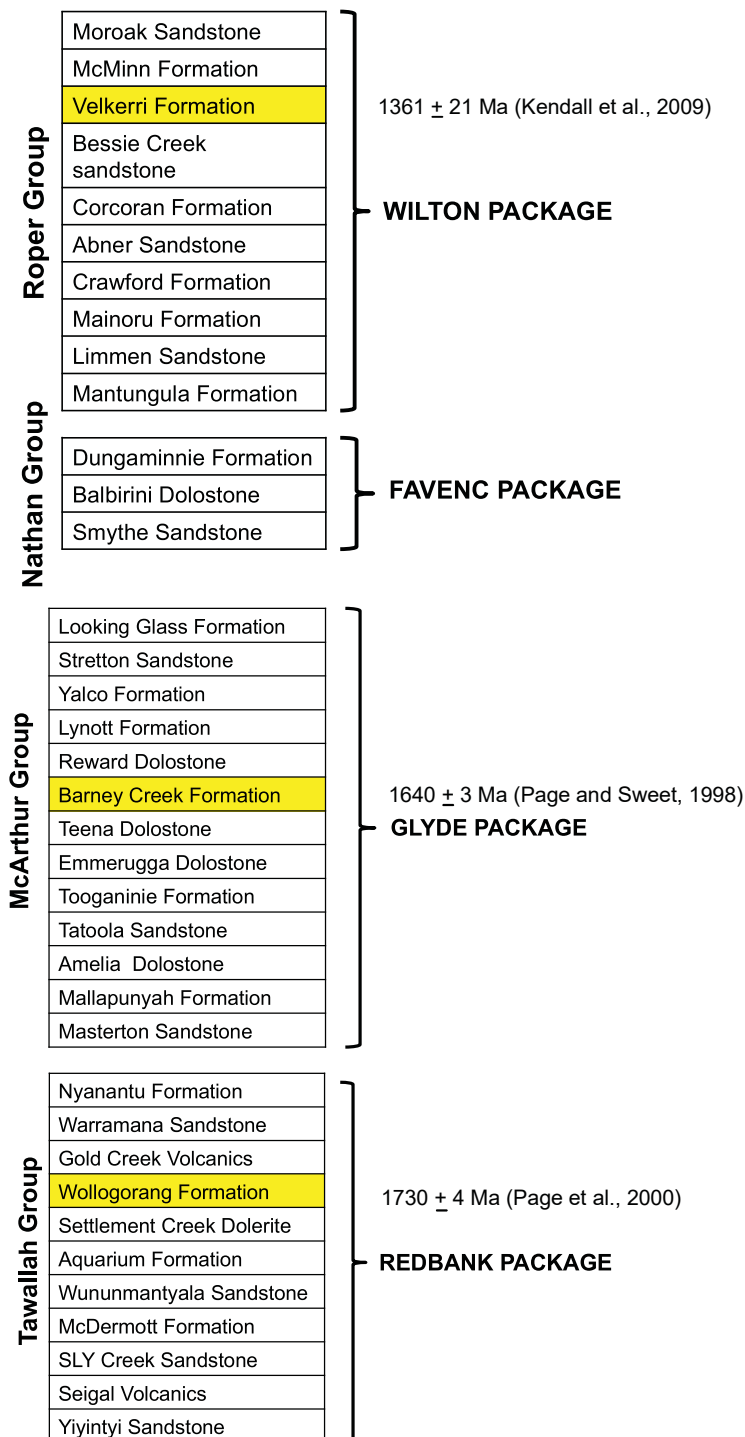
SOUTHEASTERN McARTHUR BASIN

Roper Group		
Moroak Sandstone		
McMinn Formation		
Velkerri Formation	1361 ± 21 Ma (Kendall et al., 2009)	
Bessie Creek sandstone		
Corcoran Formation	**WILTON PACKAGE**	
Abner Sandstone		
Crawford Formation		
Mainoru Formation		
Limmen Sandstone		
Mantungula Formation		

Nathan Group

Dungaminnie Formation		
Balbirini Dolostone	**FAVENC PACKAGE**	
Smythe Sandstone		

McArthur Group

Looking Glass Formation		
Stretton Sandstone		
Yalco Formation		
Lynott Formation		
Reward Dolostone		
Barney Creek Formation	1640 ± 3 Ma (Page and Sweet, 1998)	
Teena Dolostone	**GLYDE PACKAGE**	
Emmerugga Dolostone		
Tooganinie Formation		
Tatoola Sandstone		
Amelia Dolostone		
Mallapunyah Formation		
Masterton Sandstone		

Tawallah Group

Nyanantu Formation		
Warramana Sandstone		
Gold Creek Volcanics		
Wollogorang Formation	1730 ± 4 Ma (Page et al., 2000)	
Settlement Creek Dolerite		
Aquarium Formation	**REDBANK PACKAGE**	
Wununmantyala Sandstone		
McDermott Formation		
SLY Creek Sandstone		
Seigal Volcanics		
Yiyintyi Sandstone		

Fig 2 Generalized stratigraphy of the southern McArthur Basin, Australia adapted from Rawlings (1999); highlighted in yellow are the three black shale formations examined in this study.
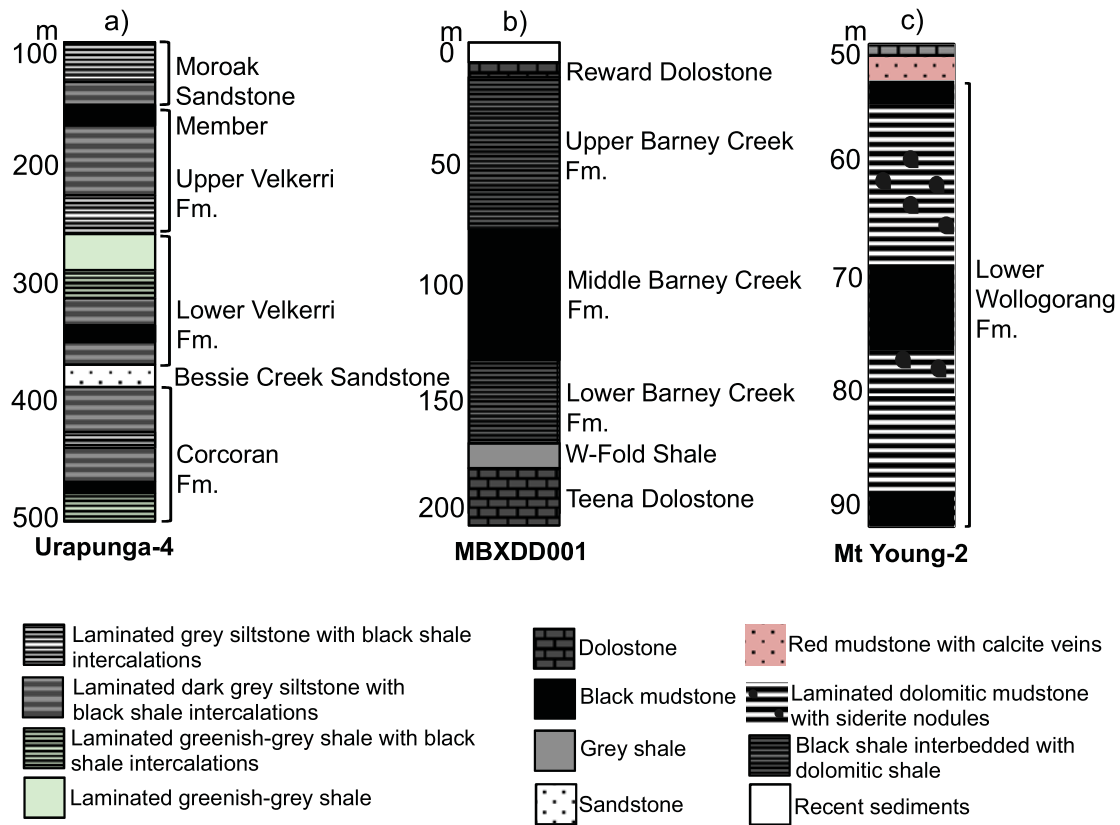
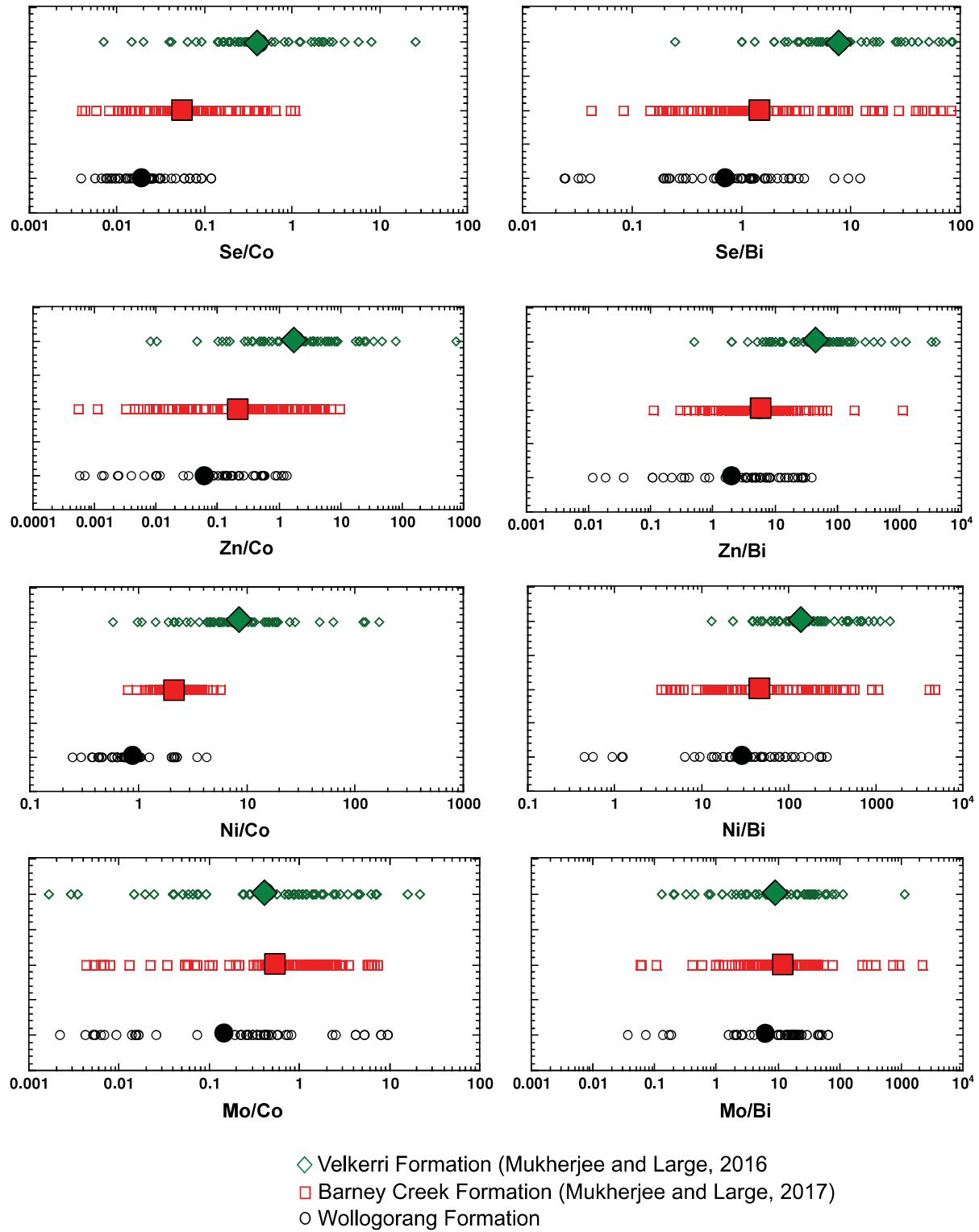Fig 3a, b, c Simplified logs of the three drill holes used for the study.

a)

◇ Velkerri Formation (Mukherjee and Large, 2016)
□ Barney Creek Formation (Mukherjee and Large, 2017
○ Wollogorang Formation

b)

◇ Velkerri Formation (Mukherjee and Large, 2016
□ Barney Creek Formation (Mukherjee and Large, 2017)
○ Wollogorang Formation
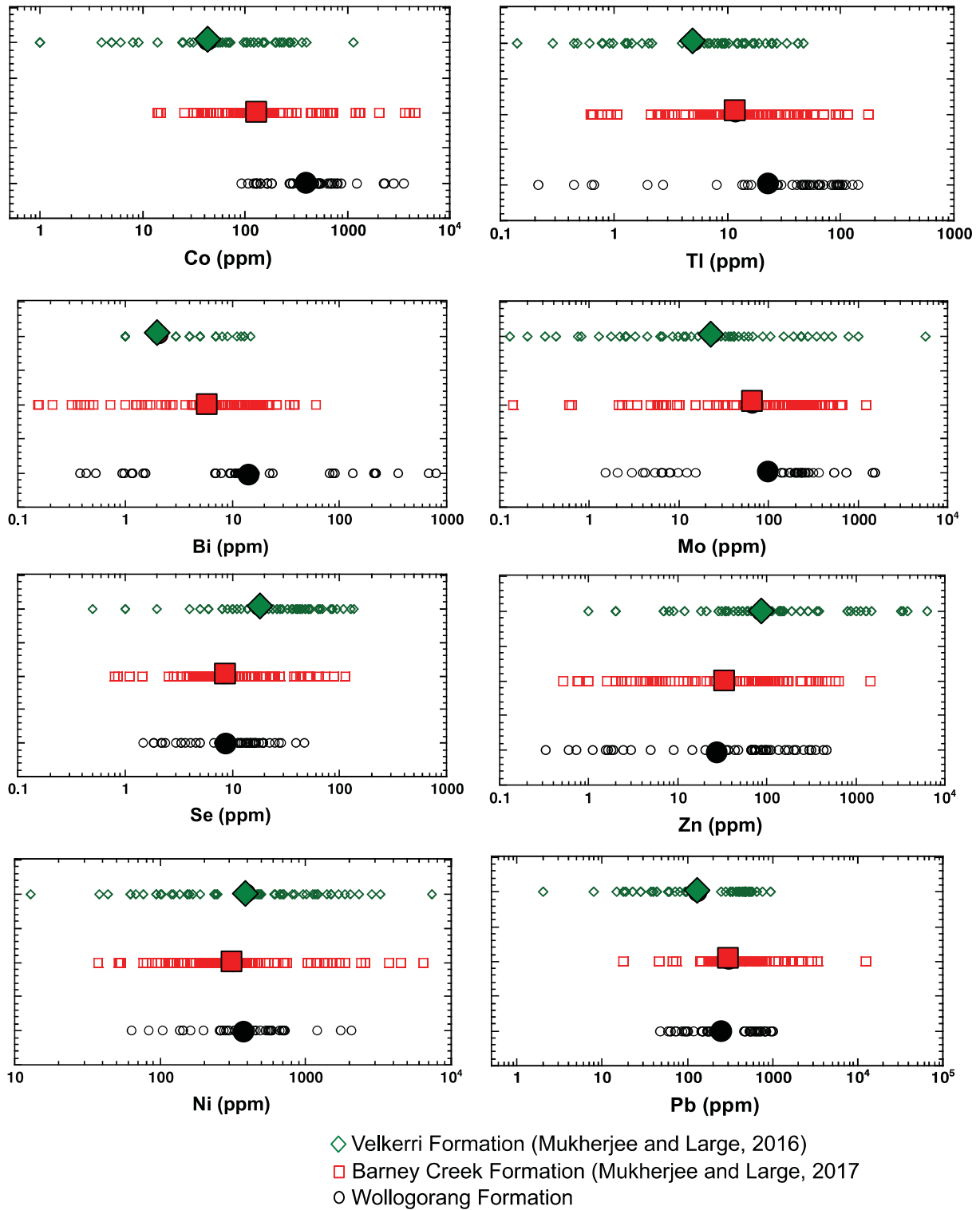
Fig 4a, b Comparison of trace elements in pyrite and their ratios in the three black shale formations
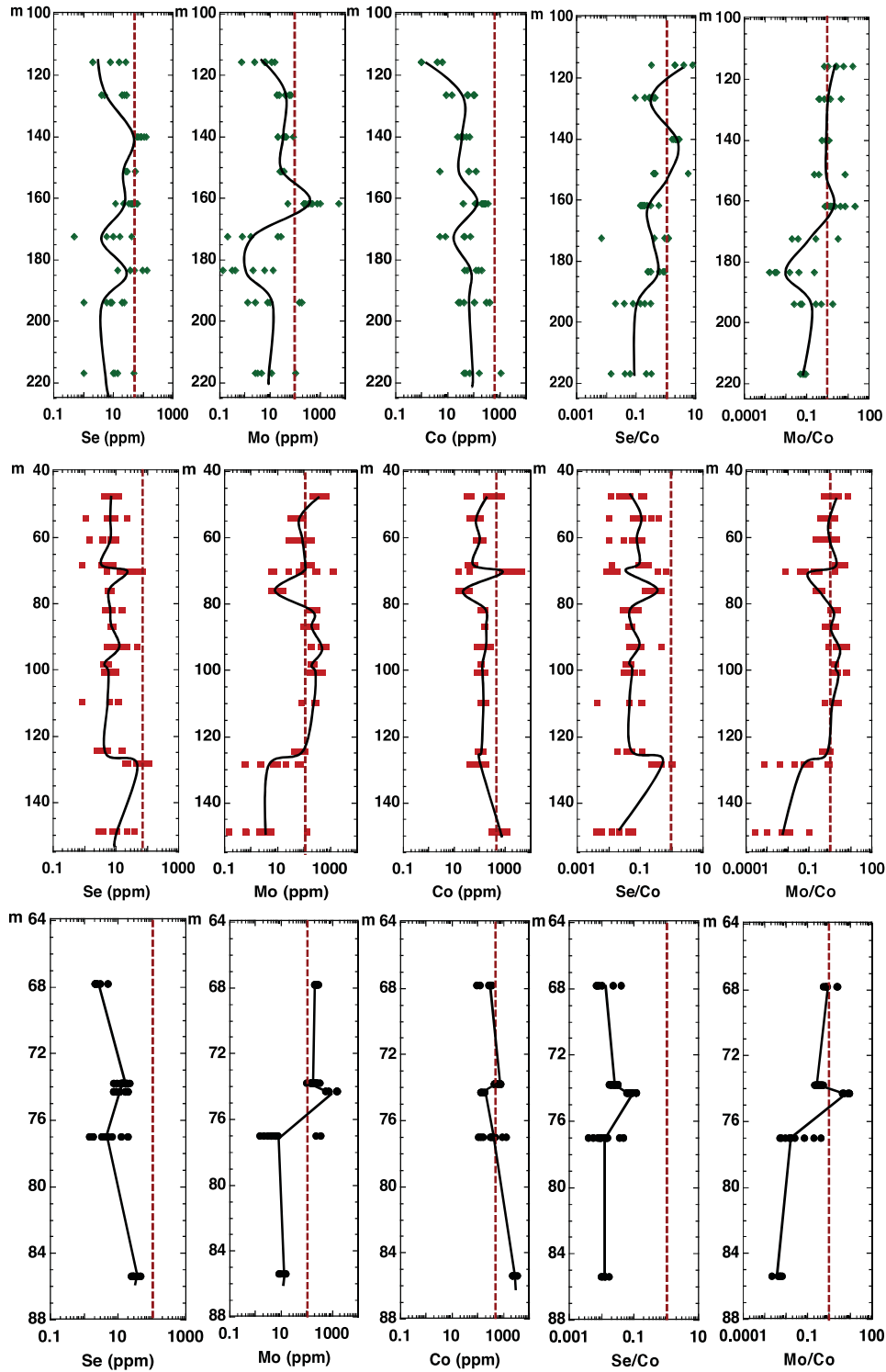
Fig 5 Downhole variation of TEs (Se, Mo, Co (in ppm) & Se/Co, Mo/Co) for the Velkerri, (top), Barney Creek (middle) and Wollogorang (bottom) formations; Red dashed line represents global mean value of ~5000 pyrites for Se, Mo, Co (from Large et al., 2014); and unity for Se/Co & Mo/Co (Data source for Velkerri Formation: Mukherjee and Large, 2016 and Barney Creek Formation: Mukherjee and Large, 2017)
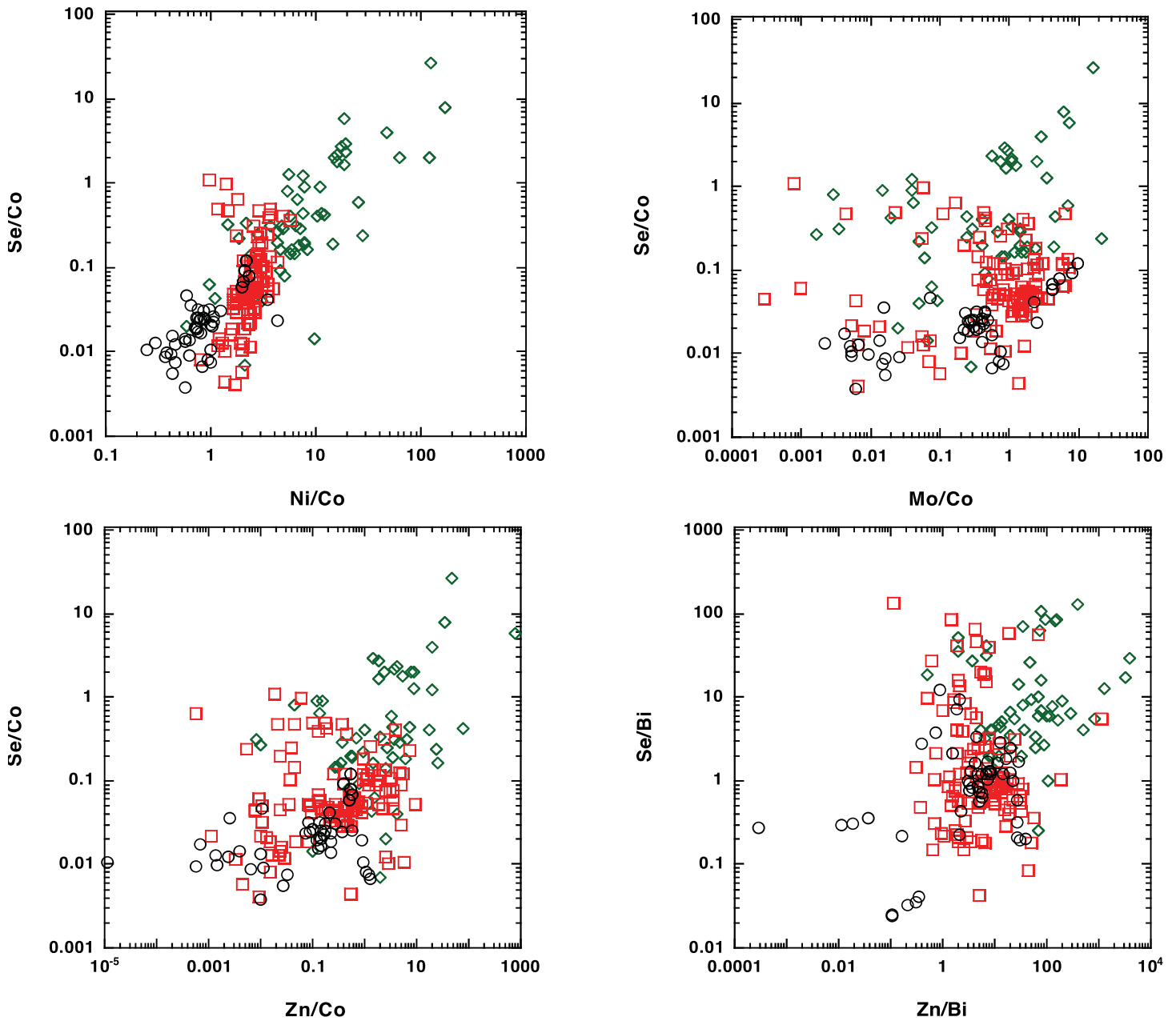
◇ Velkerri Formation (Mukherjee and Large, 2016
□ Barney Creek Formation (Mukherjee and Large, 2017)
○ Wollogorang Formation

Fig 6 Plot of Se/Co: Ni/Co; Se/Co: Mo/Co; Se/Co: Zn/Co; Se/Bi; Zn/Bi   for the three black shale formations (black circles: Wollogorang; red squares: Barney Creek; green diamonds: Velkerri)
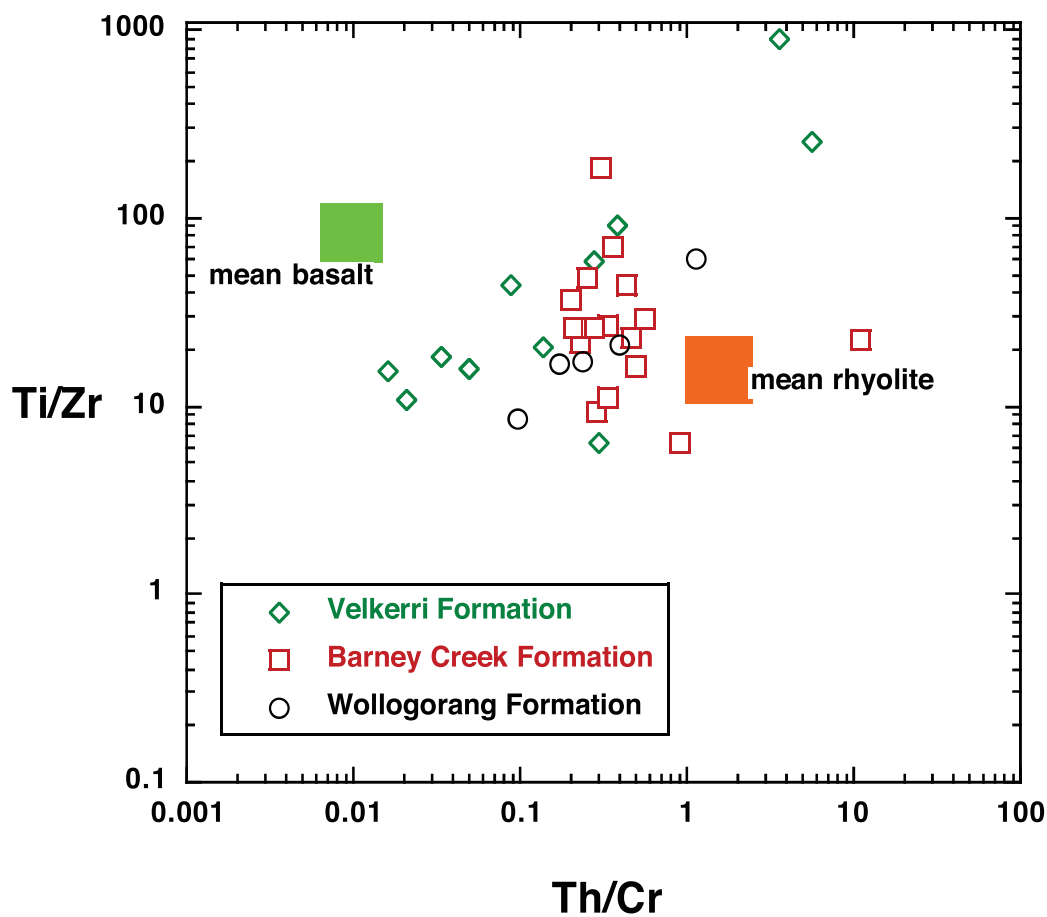
Fig 7 Plot of Th/Cr and Ti/Zr ratios for silicate matrix compositions of the black shales to identify source rock composition (felsic or mafic); Ti/Zr and Th/Cr ratios for basalt and rhyolite from Riemann and De Caritat (1998).

-23.44 to 22.35 ‰
Johnston et al., 2008

19.7 to 35.22 ‰
Johnston et al., 2008

-1.9 to 6.3 ‰
Shen et al., 2002
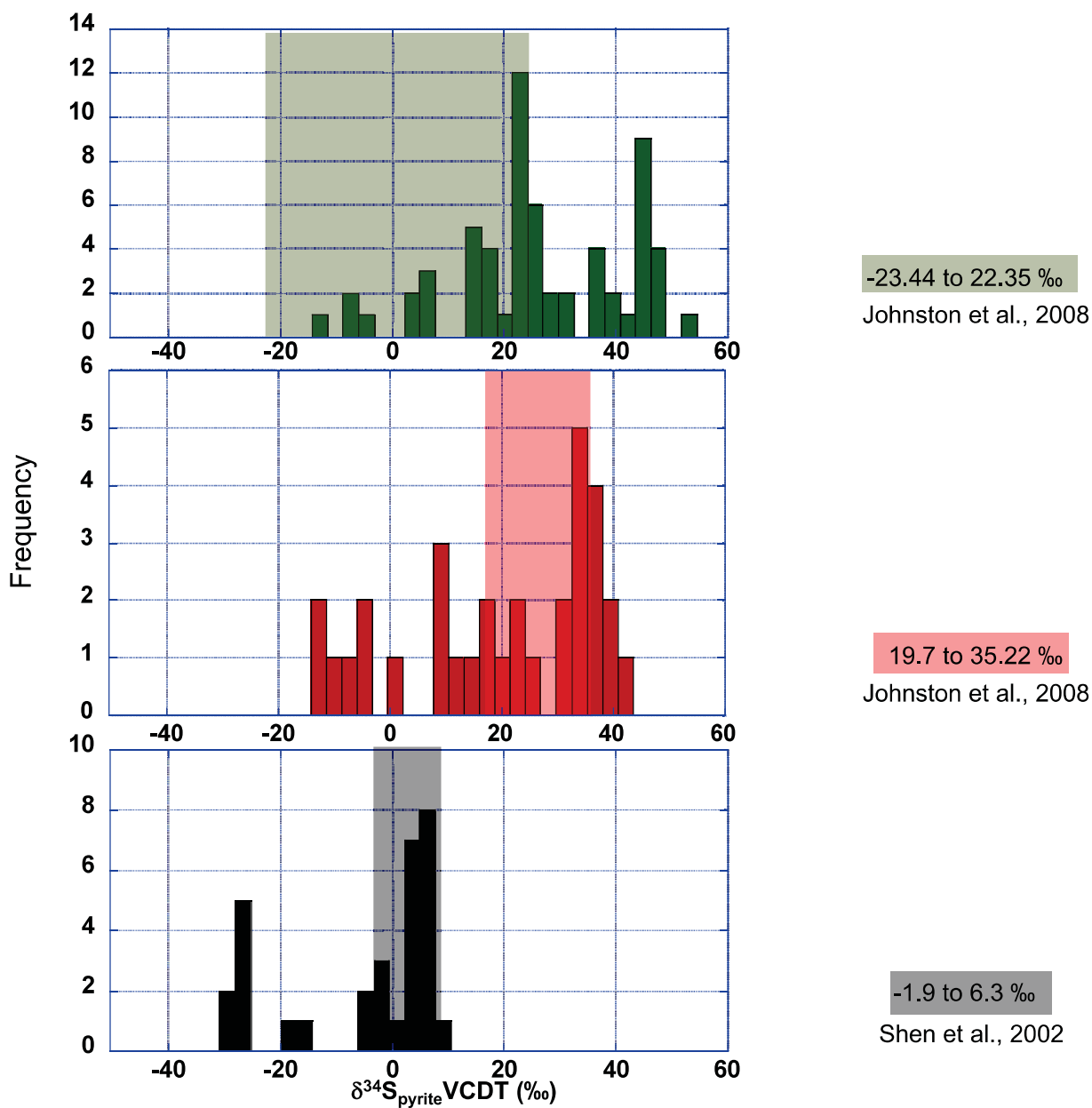
Fig 8 Pyrite sulphur isotopic compositions $\delta^{34}S_{VCDT}$ for the three black shale formations (black/bottom: Wollogorang; red/middle: Barney Creek; green/top: Velkerri); shaded regions represent range of sulphur isotopic compositions $\delta^{34}S_{VCDT}$ from Johnston 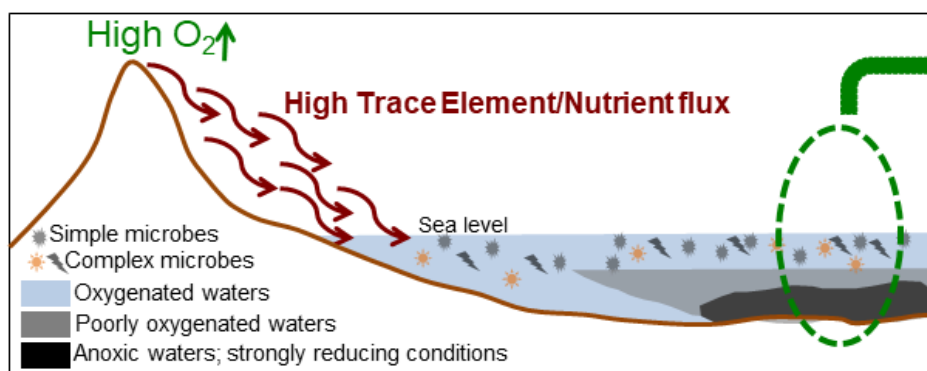et al. (2008) and Shen et al. (2002) in these formations.